The Temporal and Bilateral Structure of Hippocampal Replay

By

Stuart Pope Layton
B.S. Neuroscience
Brigham Young University, 2007

Submitted to the Department of Brain and Cognitive Science
in Partial Fulfillment of the Requirements for the Degree of

Doctor of Philosophy in Neuroscience
at the
Massachusetts Institute of Technology
JUNE 2013

Signature of Author: _____
Department of Brain and Cognitive Sciences
March 31, 2013

Certified by: _____
Matthew A. Wilson
Sherman Fairchild Professor of Neuroscience
Thesis Supervisor

Accepted by: _____
Matthew A. Wilson
Sherman Fairchild Professor of Neuroscience
Director of Graduate Education for Brain and Cognitive Sciences

The Temporal and Bilateral Structure of Hippocampal Replay

By

Stuart Pope Layton

Submitted to the Department of Brain and Cognitive Sciences
On March 31, 2013 in Partial Fulfillment of the Requirements for the
Degree of Doctor of Philosophy in Neuroscience

ABSTRACT

The hippocampus is required for the formation, but not storage, of long-term episodic memories. During memory formation, however, the hippocampus is not a lone actor; rather it works in concert with various structures across the brain. The mechanisms by which diverse populations of cells are coordinated for the formation of a single, coherent memory remain unknown. This thesis is an investigation of the temporal and hemispheric structure of replay events. The timing of replay is investigated at the levels of hippocampal sharp-wave ripples and multi-unit activity. We found that, during sleep, ripples generation is modulated by a 10-15Hz rhythm. We also observed this rhythm in the multi-unit firing rate of hippocampal neurons. Next we investigated and quantified the level of coordination between the hippocampi during replay events. Using bilateral hippocampal recordings from several rats during spatial navigation and subsequent sleep epochs, we directly compared the activity of these two spatially isolated networks at the level of the local field potential and the information encoded by the two neuronal populations. We found that the neural activity of the two hippocampi was highly correlated in some aspects but not others. As previously reported in the mouse, we found that, in the rat, sharp-wave ripples were simultaneously generated spontaneously in both hippocampi and that, although the intrinsic frequencies of ripple oscillations were correlated bilaterally, the phases of the individual ripple wavelets were not. Finally, we found that information encoded by both hippocampal ensembles is highly correlated during replay events.

Thesis Advisor: Matthew A. Wilson
Title: Sherman Fairchild Professor of Neuroscience

Acknowledgements

I'm extremely grateful to my thesis advisor Matthew Wilson for accepting me into his lab and supporting me through the entirety of my graduate studies. Working with a scientist who refuses to cut corners and values scientific integrity above all has been an extremely beneficial experience. I am determined to carry those values with me. Additionally, I'm extremely grateful for the environment of freedom that Matt fostered within his lab. While painful at time this environment was instrumental in allowing me uncover my strengths and passions.

I also need to recognize my undergraduate advisor, Scott Steffensen. Scott was able to look beyond my immaturities and recognized my potential as a member of the scientific community. He taught me how to channel my passions and started me on the path of becoming a scientist.

There are several members of the BCS community that I need to recognize. First Greg Hale and Hector Penagos. They were both instrumental in teaching me the skills required to succeed in the Wilson lab and how to execute the scientific process. Fabian Kloosterman for patiently mentoring me over the course of our collaboration. Eric Jonas for taking a naïve first year under wing and introducing him to MIT. I would not have survived MIT without Eric's friendship and wisdom. I need to thank Retsina Meyer and Andrew Bolton for countless hours spent they spent keeping me sane either through quick trips to area 4 or walks around the river.

I need to thank my parents Alan and Leslie for everything they've done in my life. They were the first to foster my curiosity and when most people would have thrown in the towel they persevered. At an early age they recognized my intellectual potential and sacrificed much to provide a stimulating and meaningful education. So much of who I am is the direct result of their love and care for me.

Lastly, I am extremely grateful for my wife and partner Aubrey. Her enduring love and undying support were invaluable in helping me achieve the impossible. Thank you.

Table of Contents

Introduction

THE HIPPOCAMPUS AND EPISODIC MEMORY

Historically, the functional role of the hippocampus was poorly understood. Early hypotheses of hippocampal function suggested it played a variety of roles ranging from olfaction to emotion (Andersen, Morris, Amaral, Bliss, & O'Keefe, 2006). However, it wasn't until doctors surgically removed the hippocampi of Henry Molaison that the hippocampus' central role in memory formation was demonstrated (Schmolck, Kensinger, Corkin, & Squire, 2002). This tragic discovery spawned decades of work intended to characterize hippocampal physiology and connect the physiology to memory formation.

The hippocampus is located in the medial temporal lobe of the mammalian brain. A close examination of the hippocampus reveals a highly structured feed-forward network. The perforant path, which arises from the entorhinal cortex (EC) and terminates in the dentate gyrus (DG), is the major input in the hippocampus. DG then sends projections to the CA3 sub-region, which in turn then projects to CA1. The projections from CA1 are the major hippocampal outputs; they terminate in EC and the subiculum. There are a few notable exceptions to this circuitry; the first is that EC sends projections directly to CA1. The second is that, in addition to projecting to CA1, CA3 pyramidal cells project to other pyramidal cells within CA3. Hippocampal circuitry is almost completely unilateral with the exception of which projects bilaterally.

The local field potential (LFP) of the hippocampus is dominated by two major states (Buzsáki, Lai-Wo S, & Vanderwolf, 1983). The first is the theta state, which is characterized by a strong 4-12 Hz oscillation in the LFP. This oscillation, commonly called the theta rhythm, is strongest during periods of navigation, attention, and REM sleep (Andersen et al., 2006; Buzsáki et al., 1983). During the theta state individual units are synchronized to the theta oscillation wit different cell types preferring different phases of the oscillation (Csicsvari, Hirase, Czurkó, Mamiya, & Buzsáki, 1999a; Klausberger et al., 2003).

The second major state in the HPC LFP is referred to as the LIA state. This state is thought to occur when the HPC is "off-line" or disconnected from its cortical inputs; such as during pauses in navigation, quiet wakefulness, and slow wave sleep (Buzsáki et al., 1983). During LIA state, the hippocampal LFP is random and contains a broad spectrum of frequencies; however, the most notable feature is the large irregular fluctuations in the LFP called sharp-waves. Individual sharp-waves are short lived (<50 ms), and are accompanied by a high-frequency (100-250Hz) oscillation called ripples (Csicsvari, Hirase, Czurkó, Mamiya, & Buzsáki, 1999b). Together these events are called sharp-wave ripples (SWR). Although individual SWR events are quite short they are frequently generated in sets with some sets containing more than 5 individual SWR and lasting more than 500ms (Csicsvari, Hirase, Czurkó, Mamiya, & Buzsáki, 1999b; Davidson, Kloosterman, & Wilson, 2009). HPC unit-activity is dramatically different during the LIA state; the majority

of the time HPC units have low irregular firing rates. However, during SWR HPC units become highly synchronized and dramatically increase their firing rate (Csicsvari, Hirase, Mamiya, & Buzsáki, 2000).

In rodents, the principle cells of the hippocampus exhibit place-specific tuning, meaning that their firing rate is a function of the animal's location in space (O'Keefe & Dostrovsky, 1971; Wilson & McNaughton, 1993). The interesting tuning properties are the source of the name place-cells. The connection between the physiology of place-cells and memory formation becomes apparent during navigation. As a rodent moves in space, neurons in its HPC are sequentially activated, with individual sequences representing very specific trajectories. Later during pauses in navigation, HPC place-cells will spontaneously reactivate in the same sequences that were observed during navigation (Diba & Buzsáki, 2007; Foster & Wilson, 2006; Lee & Wilson, 2002). The expression of these sequences demonstrates that at some level the HPC actively maintains an internal representation of recent experience.

These findings fit well with a popular model of hippocampal memory formation. The model proposes two stages in the process of memory formation and suggests different functions for each stage (Buzsáki, 1989). During the first, or learning stage, the HPC receives and stores information from cortex. Later, during breaks in the learning stage, information stored temporarily by the HPC is transferred to

cortex for permanent storage. The described physiology of the hippocampus fits this model well.

Several groups have found evidence that HPC reactivation is involved in the formation of long-term memories. These groups independently demonstrated that the disrupting HPC reactivation had a negative impact on the behavioral correlates of learning (Ego-Stengel & Wilson, 2010; Girardeau, Benchenane, Wiener, Buzsáki, & Zugaro, 2009; Jadhav, Kemere, German, & Frank, 2012). These groups also demonstrated that the disruption of learning was specific to the task at hand and did not reflect a decreased ability to learn in general.

CHAPTER OVERVIEW

The focus of this thesis is divided across three distinct but inter-related chapters, a brief overview of each chapter follows:

Chapter 2: Bilateral synchrony of the hippocampi during replay events is directly studied. Hippocampal replay is of scientific interest because it's a candidate mechanism for the hippocampal dependent of consolidation long-term episodic memories. Using electrophysiological recordings from both hippocampi we directly investigate the synchrony between the structures at the level of single units and at the level of the local field potential. We observe that many features of both the local field potentials are highly correlated between the hemispheres; particularly the timing of sharp-wave ripple generation and the frequency of ripple oscillations. The most impactful result is the discovery that information encoded in the spiking activity of both hippocampal populations is strongly correlated. These results provide a detailed characterization of the bilateral interactions between the hippocampi and lay the groundwork for further bilateral hippocampal experiments.

Chapter 3: This chapter focuses on the timing of ripple event-generation by the hippocampus. Ripples are frequently observed as pairs, triplets, or longer sets; however, the within-set timing of ripple events remains unknown. This chapter presents results that demonstrate that ripple generation is modulated by a 10-15 Hz rhythm. Furthermore, a 10-15hz rhythm is observed in the firing rates of

hippocampal neurons during ripple events. Next, we demonstrate that unit activity in retro-splenial cortex is correlated with unit activity in the hippocampus and modulated by ripple events in CA1. Lastly we provide preliminary results demonstrating that activity in retro-splenial cortex synchronizes better with slower ripple events.

Chapter 4: In this chapter we propose a novel algorithm for decoding neuronal spiking activity. Neuronal decoding is a useful technique for both medical and scientific reasons. This method has potential applications in both realms due to its simple nature and ability to produce highly accurate estimates. Briefly, this method can operate unsorted multi-unit activity, circumventing the spike-sorting process. This is done by decoding information from the spike-waveform features directly, rather than clustering. The accuracy of our new method is tested and the accuracy of other commonly used methods are provided as a benchmark. Finally, we demonstrate that our method can be used for real-time on-line decoding by directly assessing its accuracy under simulated on-line conditions.

REFERENCES

Andersen, P., Morris, R., Amaral, D., Bliss, T., & O'Keefe, J. (2006). *The Hippocampus Book*. Oxford University Press, USA.

Buzsáki, G. (1989). Two-stage model of memory trace formation: a role for "noisy" brain states. *Neuroscience*, *31*(3), 551–570.

Buzsáki, G., Lai-Wo S, L., & Vanderwolf, C. H. (1983). Cellular bases of hippocampal EEG in the behaving rat. *Brain Research Reviews*, *6*(2), 139–171. doi:10.1016/0165-0173(83)90037-1

Csicsvari, J., Hirase, H., Czurkó, A., Mamiya, A., & Buzsáki, G. (1999a). Oscillatory coupling of hippocampal pyramidal cells and interneurons in the behaving Rat. *The Journal of Neuroscience*, *19*(1), 274–287.

Csicsvari, J., Hirase, H., Czurkó, A., Mamiya, A., & Buzsáki, G. (1999b). Fast network oscillations in the hippocampal CA1 region of the behaving rat. *The Journal of Neuroscience : the Official Journal of the Society for Neuroscience*, *19*(16), RC20.

Csicsvari, J., Hirase, H., Mamiya, A., & Buzsáki, G. (2000). Ensemble patterns of hippocampal CA3-CA1 neurons during sharp wave-associated population events. *Neuron*, *28*(2), 585–594. doi:10.1016/S0896-6273(00)00135-5

Davidson, T. J., Kloosterman, F., & Wilson, M. A. (2009). Hippocampal replay of extended experience. *Neuron*, *63*(4), 497–507. doi:10.1016/j.neuron.2009.07.027

Diba, K., & Buzsáki, G. (2007). Forward and reverse hippocampal place-cell sequences during ripples. *Nature Neuroscience*, *10*(10), 1241–1242. doi:10.1038/nn1961

Ego-Stengel, V., & Wilson, M. A. (2010). Disruption of ripple-associated hippocampal activity during rest impairs spatial learning in the rat. *Hippocampus*, *20*(1), 1–10. doi:10.1002/hipo.20707

Foster, D. J., & Wilson, M. A. (2006). Reverse replay of behavioural sequences in hippocampal place-cells during the awake state. *Nature*, *440*(7084), 680–683. doi:10.1038/nature04587

Girardeau, G., Benchenane, K., Wiener, S. I., Buzsáki, G., & Zugaro, M. B. (2009). Selective suppression of hippocampal ripples impairs spatial memory. *Nature Neuroscience*, *12*(10), 1222–1223. doi:10.1038/nn.2384

Jadhav, S. P., Kemere, C., German, P. W., & Frank, L. M. (2012). Awake hippocampal sharp-wave ripples support spatial memory. *Science*, *336*(6087), 1454–1458. doi:10.1126/science.1217230

Klausberger, T., Márton, L. F., Baude, A., Roberts, J. D. B., Magill, P. J., & Somogyi, P. (2003). Spike timing of dendrite-targeting bistratified cells during hippocampal network oscillations in vivo. *Nature Neuroscience*, *7*(1), 41–47. doi:10.1038/nn1159

Lee, A. K., & Wilson, M. A. (2002). Memory of sequential experience in the hippocampus during slow wave sleep. *Neuron*, *36*(6), 1183–1194.

O'Keefe, J., & Dostrovsky, J. (1971). The hippocampus as a spatial map. Preliminary evidence from unit activity in the freely-moving rat. *Brain Research*, *34*(1), 171–175.

Schmolck, H., Kensinger, E. A., Corkin, S., & Squire, L. R. (2002). Semantic knowledge in patient H.M. and other patients with bilateral medial and lateral temporal lobe lesions. *Hippocampus*, *12*(4), 520–533. doi:10.1002/hipo.10039

Wilson, M. A., & McNaughton, B. L. (1993). Dynamics of the hippocampal ensemble code for space. *Science*, *261*(5124), 1055–1058.

Hippocampal Replay is Bilaterally Coordinated

ABSTRACT

The hippocampus is required for the formation, but not storage, of long-term episodic memories. During memory formation, however, the hippocampus is not a lone actor; rather it works in concert with various structures across the brain. The mechanisms by which diverse populations of cells are coordinated for the formation of a single, coherent memory remain unknown. To investigate how neural activity across the brain is coordinated for episodic memory formation we examined the bilateral coordination of activity between the two hippocampi. Using bilateral hippocampal recordings from 3 rats during spatial navigation and subsequent sleep epochs, we directly compared the activity of these two spatially isolated networks at the level of the local field potential and the information encoded by the two neuronal populations. We found that the neural activity of the two hippocampi was highly correlated in some aspects but not others. As previously reported in the mouse, we found that, in the rat, sharp-wave ripples were simultaneously generated spontaneously in both hippocampi and that, although the intrinsic frequencies of ripple oscillations were correlated bilaterally, the phases of the individual ripple wavelets were not. Finally, we found that information encoded by both hippocampal ensembles is highly correlated during replay events.

INTRODUCTION

The hippocampus is essential for the formation of long-term episodic memories (Tauber, 1992), though the neural mechanisms of episodic memory formation are still unknown. Attempts to elucidate this mechanism have focused on the spiking activity of neurons in the hippocampal formation. In rodents, the principal neurons in the hippocampus, often referred to as place-cells, are tuned to the animal's current location in space (O'Keefe and Dostrovsky, 1971; Wilson and McNaughton, 1993), and navigation sequentially activates groups of neurons within the hippocampus. These sequences form during the initial exposure to novel environments and are robust across time. Interestingly, during stops in exploration and during sleep, neurons in the hippocampus spontaneously express sequences corresponding to behaviorally relevant trajectories (Nádasdy et al., 1999; Foster and Wilson, 2006; Diba and Buzsáki, 2007; Karlsson and Frank, 2009; Gupta et al., 2010). The spontaneous re-expression of these behaviorally relevant sequences is called hippocampal replay/reactivation.

Replay events are temporally coupled with oscillations in the local-field potential called sharp-wave ripples(Foster and Wilson, 2006). These events are short lived and contain a high-frequency (100-250 Hz), short-lived (< 50 ms)(Ylinen et al., 1995). In fact, spikes observed during a sharp-wave ripple are phase-locked to the ripple oscillation(Ylinen et al., 1995; Csicsvari et al., 1999a; Klausberger et al., 2003), suggesting a mechanistic link between the two. Electrical stimulation of the

hippocampus during sharp-wave ripples disrupts replay and negatively affects the behavioral correlates of learning (Girardeau et al., 2009; Ego-Stengel and Wilson, 2010; Jadhav et al., 2012). Replay is well poised to play a central role in the formation of hippocampal dependent memory formation.

Lesion studies have suggested that the hippocampus does not store long-term memories, rather it temporarily stores information for later consolidation distributed in cortical networks (Buzsáki, 1998; Klausberger et al., 2003). Activity correlated with hippocampal replay has been observed in the cortex and subcortical structures (Ji and Wilson, 2008; Lansink et al., 2009; Peyrache et al., 2009; Logothetis et al., 2012). These cross-structural relationships have been observed at the level of unit activity, in the local field potentials, and in the BOLD response in humans. Sharp-wave ripples in the hippocampus have also been shown to be temporally coupled with oscillations in the cortex (Siapas and Wilson, 1998; Sirota et al., 2003; Mölle et al., 2006). Finally, reactivation of cortical sequences has been observed during the reactivation of hippocampal sequences, with a correlated content represented by the two events (Ji and Wilson, 2007). These results show that replay is a global phenomenon that recruits and coordinates the activity of networks distributed across the brains. However the mechanism responsible for coordinating spatially distributed networks are unknown.

Episodic memories can form despite cortical lesions, whereas lesions to the hippocampus disrupt episodic memory formation(Tauber, 1992; Kim and Frank, 2009). These results suggest that mechanism could reside in the hippocampus as well as the finding that the hippocampus is capable of generating replay-like events in the absence of cortical inputs (Behrens et al., 2005; Maier et al., 2009). Additionally the disruption of internal hippocampal circuitry alters frequency of ripple events(Nakashiba et al., 2008). Nevertheless, there is evidence suggesting that cortical inputs into the hippocampus may determine the timing and content of replay events. Ripples in the hippocampus are temporally correlated with spindles in cortex; however, spindles in cortex tend to precede ripples in the hippocampus (Penagos, 2010), these results indicate that cortical precedes replay in the hippocampus, suggesting replay maybe responding to cortical drive. Additional evidence for this hypothesis is that, during sleep, the content expressed during hippocampal replay can be directly biased by cortical inputs(Bendor and Wilson, 2012).

Investigation of bilateral synchronization of the hippocampi during replay events is an appropriate point to begin studying the mechanisms responsible for coordinating replay events across the brain. If hippocampal replay is bilaterally coordinated, there is likely a common driver that is either intrinsic to the hippocampus (e.g., via the hippocampal commissure) or external, area sending common projections to the hippocampus (e.g., thalamus). Conversely, if bilateral replay events are

uncoordinated, anatomically separate inputs to each hippocampus are likely driving the individual events. To first understand the level of coordination between the two hippocampi, we simultaneously recorded from both hippocampi during sleep and while animals performed a spatial navigation task for a small food reward. We observed that content and timing of hippocampal replay events are highly correlated between the two hippocampi. Additionally we demonstrate that replay events that recruit a greater number of neurons are more correlated than events that recruit few units. Lastly we verify previously published work demonstrating that sharp-wave ripples are simultaneously generated by both hippocampi, but that bilateral ripples are not coordinated in phase. We extend these results by demonstrating that frequency of ripples is bilaterally correlated. These data will help shape future studies to elucidate the source(s) of this coordination.

RESULTS

Sharp-Wave Ripples

The synchrony of bilateral ripple generation was studied in 3 rats during periods of sleep (SLEEP) and pauses in navigation (PAUSE). Sharp-wave ripples were detected simultaneously in both hippocampi, confirming previous studies in mice(Buzsáki et al., 2003). Sharp-wave ripples were independently detected (**Figure 2A**) on multiple channels of LFP recorded from both hippocampi (**Figure 2B**). Simultaneous ripple events were not detected in all cases, likely due to distance between electrodes, noisy signals, or an imperfect ripple detection algorithm. The probabilities of detecting coincident ripples on ipsilateral electrodes (PAUSE: 0.45 +/- 0.11, SLEEP: 0.75 +/-0.06) and contralateral pairs (PAUSE: 0.380 +/- 0.11, SLEEP: 0.70 +/- .03) were not significantly different (**Figure 2C**). The probabilities of observing ipsilateral pairs are similar to previously reported numbers(Csicsvari et al., 2000). The higher probabilities during sleep are likely the result of increased ripple amplitude during SLEEP compared to PAUSE.)
Ripple-triggered averages of the local field potential revealed sharp-waves for both ipsilateral and contralateral electrode pairs; however, the ripple oscillation was only revealed for ipsilateral comparisons. The phase of the ripple oscillation is correlated within (**Figure 3C**) but not between (**Figure 3D**) the hippocampi (Buzsáki et al., 2003), explaining the failure of the triggered averages to capture the contralateral ripple oscillation. The frequencies of ripple oscillations; however, is correlated both

within (r_{run} = 0.497 and r_{sleep} 0.607) and between the hippocampi (r_{run} = 0.312 and r_{sleep} 0.367) (**Figure 3A,B)**.

These results verify previous reports of simultaneous ripple generation by both hippocampi, but they extend those results by demonstrating that the frequency of the ripple oscillation is correlated between the hippocampi. Exactly how the ripple frequency is not likely the result of common network dynamics internal to CA1; however, consistency in the frequency could be the result of the common CA3 inputs between hippocampi via the hippocampal commissure, as eliminating neurotransmitter release from CA3 pyramidal cells results in altered ripple frequency but not incidence (Nakashiba et al., 2009).

Multi-Unit Activity

The link between hippocampal unit activity and ipsilateral ripples is well documented (Csicsvari et al., 1999b; 2000). Here we found that the unit activity and sharp-wave ripples is maintained between the two hemispheres, consistent with the coincident occurrence of ripples. The firing rate of hippocampal units increased dramatically during sharp-wave ripples in the opposite hippocampus (**Figure 4A**), and the mean hippocampal multi-unit firing rate triggered on ripples in the contralateral hemisphere demonstrates the magnitude of this relationship **(Figure 4B)**. Bursts in the hippocampal during PAUSE and SLEEP multi-unit activity were highly correlated between the hemispheres. **(Figure 4C)**. The strong correlations of

hippocampal unit activity during sharp-wave ripples are not surprising given the ripple synchrony results. Lastly, the mean firing rate during individual bursts in the multi-unit activity were significantly correlated (*r=0.589*), indicating that events strongly or weakly recruit activity in both hemispheres.

Independent Position Decoding for Each Hippocampus

Activity in either hippocampus can be decoded to produce position estimates. We found that the independently computed position estimates from both hippocampi were very similar. Establishing the level of similarity between run decoding estimates is crucial, as the run is used as a template for replay decoding. Confusion matrices constructed from the both estimates showed a strong diagonal structure, indicating a high level of agreement between the two estimates (**Figure 5B**). In addition, the confusion matrices for all analyzed sets were significantly more precise ($p < 4.052\text{x}10^{-9}$ one-sided t-Test) than expected by chance (**Figure 5C**). Finally, estimates at each time-bin were highly correlated (**Figure 5D),** and the distribution of correlations between the hemispheres for all animals was significantly better than expected by chance ($p < 2.499\text{x}10^{-12}$ one-sided t-Test).

Bilateral Replay Decoding

The spiking activity observed during sharp-wave ripples can be decoded to a reveal trajectory-like structure (Davidson et al., 2009). We used this previously described method to evaluate data recorded from both hippocampi. Independent decoding of

the activity in both hippocampi during putative replay events yielded qualitatively similar trajectories (**Figure 6A**). Examples shown in Figure 6 demonstrate that the information encoded by the two hippocampi was correlated for a significant fraction of the replay events. These results are important as the correlation of information lasts for periods of time, suggesting that the information encoded by both hippocampi changes over time in a bilaterally coherent manner. Not only are the visually identifiable trajectories highly correlated but events lacking obvious structure were correlated as well. As a population, replay events were significantly (PAUSE $p<[3.10\text{x}10^{-26} / 0.034]$, SLEEP $p<[2.21\text{x}10^{-25} / 0.21]$, [best/worst]-case, 2 sample KS-Test) more correlated between the hippocampi than would be expected if the two hippocampi were expressing randomly selected, behaviorally relevant trajectories of the same length (**Figure 6B**). This relationship was true for all analyzed data sets and was stronger during PAUSE than SLEEP. One potential explanation for higher event correlations during PAUSE is that SLEEP replay events were decoded using PAUSE as a template, and replay events during SLEEP could potentially represent a greater number of environments. In addition, spike sorting errors and incorrectly matching cell identities between PAUSE and SLEEP epochs will decrease the quality of the decoded position estimates (Goodman and Johnson, 2008); inaccurate estimates of replay content will thus have lower bilateral correlations.

No examples of de-correlated replay estimates were found, this absence could be the result of either improper sampling of the hippocampal populations or rather de-correlated bilateral replay might rarely, if ever, occur. The variance of decoded replay estimates is inversely proportional to the number of spikes observed during potential replay events (Zhang et al., 1998; Davidson et al., 2009). Therefor de-correlated replay events are more likely to be detected during high rate events (events with many active neurons) as opposed to low rate events (events with few active neurons), as inconsistencies between the decoded positions are less likely to be the result of incomplete sampling. On average, the strength of event correlations increased as a function of the mean unsorted multi-unit firing during an event (**Figure 6D**). For all data sets, events containing more than 50% maximal activity were significantly more correlated than events with less than 50% maximal activity (p<0.024 paired rank-sum test) (**Figure 6E**). These results, coupled with the absence of examples of de-correlated bilateral replay events suggest that de-correlated replay occurs rarely, if at all.

DISCUSSION

This paper provides evidence that sharp-wave ripple events are simultaneously generated by both hippocampi. While previous publications have demonstrated bilateral coordination in ripple timing (Buzsáki et al., 2003). This study demonstrates for the first time that the frequency of the ripple oscillation within a sharp-wave ripple event is correlated between the hippocampi. The frequencies of non-coincident ripples events are not correlated demonstrating that in CA1 ripple frequency isn't simply a function of internal network dynamics but that the ripple frequency is modulated in part by upstream structures. The identity of this upstream network is currently unknown, although there is evidence that it could be CA3 (Finnerty and Jefferys, 1993; Buzsáki et al., 2003). However further work needs to be done before a definitive statement can be made.

This paper also demonstrates information encoded in the population activity of both hippocampi is correlated replay events. Previous work has shown that decoding the combined activity of both hippocampi during replay produces behaviorally relevant trajectories, but failed to explicitly investigate the relationship between the two spatially distant populations. These studies were conducted under the assumption that activity in the two structures is correlated; an assumption that is validated by the results in this paper. In addition to validating this assumption, this work lays

the groundwork for further studies into the mechanisms governing the content and timing of replay events.

Two potential mechanisms could explain the results of this paper. The first is that CA3 is responsible for triggering ripples and dictating coordinating the content of the replay event. Some models of sharp-wave ripple generation hypothesize that ripples are strong inputs from CA3 trigger ripples in CA1. The sharp-wave component of sharp-wave ripples events is hypothesized to be generated by synchronized inputs into CA1 from CA3 (Ylinen et al., 1995). As the output of CA3 projects bilaterally to both hippocampi, through the hippocampal commissure, CA3 is well poised to act as the agent responsible for bilaterally synchronizing CA1. However, it's unclear if CA3 plays this role and bridges disparate information between the hippocampi. An alternative is that the cortical inputs into the hippocampus are already synchronized between the hemispheres and the synchrony observed in CA1 is the result of coherent cortical inputs.

The role CA3 in synchronizing the content and timing of replay can be directly tested with a lesion experiment. Severing the hippocampal commissure, which contains the decussating CA3 output, will disconnect the two hippocampi while preserving the structure their internal networks. Following this procedure any bilateral synchrony of CA1 must be the result of common cortical inputs into both hippocampi; this structure, or lack thereof, can be used to infer if the mechanisms

responsible for coordinating the content and timing of replay events lie within the hippocampus or exist in upstream networks.

METHODS

Electrophysiology and Behavior

Three male Long-Evans rats, weighing between 400 and 600 grams, were implanted with micro-drive arrays containing either 24 (R1, R2) or 30 (R3) independently movable tetrodes targeted at dorsal CA1 and CA3 bilaterally. Following a successful surgery each tetrode was slowly lowered into the brain until they reached the cell-layer of the target structure. A tetrode was placed in white matter dorsal to CA1 to serve as a reference. At the conclusion of the experiment electrode placement was verified using electrolytic lesions. Signals from the tetrodes were split into spike and local field potential channels. Spike channels were filtered between 300 Hz - 6 kHz. Extra-cellular action potentials were detected as threshold crossings on any tetrode channel, and a 32-sample spike waveform for each channel was recorded for each threshold crossing. Local field potential signals were filtered between 0.5 and 475 Hz and sampled at 1500 Hz.

Following successful electrode placement the rats were food deprived to 85% of the baseline weights and received a food rewards for navigating a 3.1-meter linear track (R1, R2) or within a W-track (R3) environment. An overhead video camera and infrared light emitting diodes mounted on the implanted micro-drive array were used to track the rats' position. All experiments were conducted in accordance with the guidelines of the US National Institute of Health, and under the supervision of their respective animal care facilities.

Sharp-wave Ripple Detection and Analysis

The three tetrodes with the greatest number of units were selected for ripple analysis, with at least one tetrode from each hippocampus. Of the three, the tetrode with the most isolated units was designated as the trigger tetrode. Ripple events were detected on each tetrode using the envelope of the band-pass filtered (150 to 250 Hz) local field potential. The absolute value of the Hilbert transform was used to estimate the envelope of a signal. Periods of time when the envelope exceeded 7 SD above the mean were classified as candidate events. This is a variation of a previously described method (Csicsvari et al., 2000).

The probability of detecting coincident ripples was computed as:

$$P(detect) = \frac{nRipple_{Trig\ \&\ Test}}{nRipple_{Trig}}$$

Only ripples detected on the trigger channel that overlapped with events on test channels were used in the subsequent analysis. The peak of a ripple event was detected as the sample of the band-pass filtered LFP with the greatest value within the event. The mean frequency for each ripple was computed from average wavelength of the ripple oscillation between 25ms before and 25 ms after the ripple peak. The phase of the ripple oscillation was estimated using the angle of the Hilbert transformed band-pass filtered signal. The sharp-wave for each ripple event was isolated by band-pass filtering the raw LFP between 0.1 and 40 Hz.

Multi Unit Burst Detection and Analysis

Peaks in the multi-unit firing rate were identified using similar methods to Davidson 2009. The multi-unit firing rate was estimated using a smoothed histogram (5ms bins; Gaussian kernel 10ms SD) of the unsorted multi-unit activity. Bursts in the multi-unit firing rate were computed using a dual threshold algorithm. Periods when the multi-unit rate exceeded a high threshold (4 SD above the mean) where flagged as candidate events. Event times were expanded until the rate dropped below a low threshold (0.5 SD above the mean). Multi-unit bursts were only computed during periods of immobility (velocity <5 cm/s)

Computing Tuning Curves

The environment was linearized and divided into 10 cm spatial bins. Tuning curves were calculated computed as a smoothed histogram (10cm bins; Gaussian kernel 10cm SD) of occupancy corrected spike counts. For datasets on the W maze, tuning curves were calculated separately for each arm of the maze and then concatenated into a single curve.

Position Decoding

Single units were segregated into two groups, one for each hippocampus, and position estimates were computed using a Bayesian reconstruction algorithm(Zhang et al., 1998).This algorithm produces a probability distribution of positions from spiking. Navigation was decoded by dividing the experiment non-overlapping 250ms time-bins.

The similarity of navigation position estimates was computed in two ways. Time-bins when the animal was stationary (velocity <15 cm/sec) were excluded from navigational analysis. A confusion matrix of the two estimates was computed using a 2D histogram of the peak of the pdf from each hemisphere for all time-bins when the animal was moving >15cm/sec. For each time-bin the mode of both pdfs was computed and the combinations of modes were counted. The precision of the confusion matrix was calculated by counting the of time-bins where the modes of both pdfs were within 20 cm of each other divided by the total number of time-bins. The correlation between the position estimates was computed on a time-bin-by-time-bin basis. A null distribution of correlations was computed by randomly circularly shifting the left estimate decoded forwards or backwards in time.

Replay Position Decoding

Candidate replay events were decoded using the same methods as run, but with non-overlapping 20ms time-bins. The correlation between events was computed as the mean time-bin correlation but only for time-bins with spikes in both hemispheres. Events with no spikes in either hemisphere were not analyzed. A null distribution of event correlations was computed by randomly shuffling events in one hippocampus with ipsilateral events of the same length. The distribution of event correlations was then computed for the real vs. shuffled event pairs. The mean multi-unit firing rate of each hemisphere was computed for each event and events

were segregated into 10 groups of increasing firing rate. High and low rate events were defined as events when the multi-unit firing rate was greater than or less than the median firing rate for all candidate events in that dataset.

REFERENCES

Behrens CJ, van den Boom LP, de Hoz L, Friedman A, Heinemann U (2005) Induction of sharp wave–ripple complexes in vitro and reorganization of hippocampal networks. Nature Neuroscience 8:1560–1567.

Bendor D, Wilson MA (2012) Biasing the content of hippocampal replay during sleep. Nature Neuroscience 15:1439–1444.

Buzsáki G (1998) Memory consolidation during sleep: a neurophysiological perspective. Journal of Sleep Research 7:17–23.

Buzsáki G, Buhl DL, Harris KD, Csicsvari J, Czeh B, Morozov A (2003) Hippocampal network patterns of activity in the mouse. Neuroscience 116:201–211.

Csicsvari J, Hirase H, Czurkó A, Mamiya A, Buzsáki G (1999a) Oscillatory coupling of hippocampal pyramidal cells and interneurons in the behaving Rat. The Journal of Neuroscience 19:274–287.

Csicsvari J, Hirase H, Czurkó A, Mamiya A, Buzsáki G (1999b) Fast network oscillations in the hippocampal CA1 region of the behaving rat. J Neurosci 19:RC20.

Csicsvari J, Hirase H, Mamiya A, Buzsáki G (2000) Ensemble patterns of hippocampal CA3-CA1 neurons during sharp wave-associated population events. Neuron 28:585–594.

Davidson TJ, Kloosterman F, Wilson MA (2009) Hippocampal replay of extended experience. Neuron 63:497–507.

Diba K, Buzsáki G (2007) Forward and reverse hippocampal place-cell sequences during ripples. Nature Neuroscience 10:1241–1242.

Ego-Stengel V, Wilson MA (2010) Disruption of ripple-associated hippocampal activity during rest impairs spatial learning in the rat. Hippocampus 20:1–10.

Finnerty GT, Jefferys JG (1993) Functional connectivity from CA3 to the ipsilateral and contralateral CA1 in the rat dorsal hippocampus. Neuroscience 56:101–108.

Foster DJ, Wilson MA (2006) Reverse replay of behavioural sequences in hippocampal place-cells during the awake state. Nature 440:680–683.

Girardeau G, Benchenane K, Wiener SI, Buzsáki G, Zugaro MB (2009) Selective suppression of hippocampal ripples impairs spatial memory. Nature Neuroscience 12:1222–1223.

Goodman IN, Johnson DHASASP2I2IICO (2008) Information theoretic bounds on neural prosthesis effectiveness: The importance of spike sorting.

Gupta AS, van der Meer MAA, Touretzky DS, Redish AD (2010) Hippocampal Replay Is Not a Simple Function of Experience. Neuron 65:695–705.

Jadhav SP, Kemere C, German PW, Frank LM (2012) Awake hippocampal sharp-wave ripples support spatial memory. Science 336:1454–1458.

Ji D, Wilson M (2007) Coordinated memory replay in the visual cortex and hippocampus during sleep. Nature Neuroscience 10:100–107.

Ji D, Wilson MA (2008) Firing rate dynamics in the hippocampus induced by trajectory learning. The Journal of Neuroscience 28:4679–4689.

Karlsson MP, Frank LM (2009) Awake replay of remote experiences in the hippocampus. Nature Neuroscience 12:913–918.

Kim SM, Frank LM (2009) Hippocampal lesions impair rapid learning of a continuous spatial alternation task. PLoS ONE 4:e5494.

Klausberger T, Márton LF, Baude A, Roberts JDB, Magill PJ, Somogyi P (2003) Spike timing of dendrite-targeting bistratified cells during hippocampal network oscillations in vivo. Nature Neuroscience 7:41–47.

Lansink CS, Goltstein PM, Lankelma JV, McNaughton BL, Pennartz CMA (2009) Hippocampus leads ventral striatum in replay of place-reward information. PLoS Biol 7:e1000173.

Logothetis NK, Eschenko O, Murayama Y, Augath M, Steudel T, Evrard HC, Besserve M, Oeltermann A (2012) Hippocampal-cortical interaction during periods of subcortical silence. Nature 491:547–553.

Maier N, Nimmrich V, Draguhn A (2009) Cellular and Network Mechanisms Underlying Spontaneous Sharp Wave-Ripple Complexes in Mouse Hippocampal Slices. The Journal of Physiology 550:873–887.

Mölle M, Yeshenko O, Marshall L, Sara SJ, Born J (2006) Hippocampal sharp wave-ripples linked to slow oscillations in rat slow-wave sleep. J Neurophysiol 96:62–70.

Nakashiba T, Buhl DL, McHugh TJ, Tonegawa S (2009) Hippocampal CA3 Output Is Crucial for Ripple-Associated Reactivation and Consolidation of Memory. Neuron 62:781–787.

Nakashiba T, Young JZ, McHugh TJ, Buhl DL, Tonegawa S (2008) Transgenic

inhibition of synaptic transmission reveals role of CA3 output in hippocampal learning. Science 319:1260–1264.

Nádasdy Z, Hirase H, Czurkó A, Csicsvari J, Buzsáki G (1999) Replay and time compression of recurring spike sequences in the hippocampus. J Neurosci 19:9497–9507.

O'Keefe J, Dostrovsky J (1971) The hippocampus as a spatial map. Preliminary evidence from unit activity in the freely-moving rat. Brain Research 34:171–175.

Penagos H (2010) Interactions Between Anterior Thalamus and Hippocampus during Different Behavioral States in the Rat (Doctoral dissertation)

Peyrache A, Khamassi M, Benchenane K, Wiener SI, Battaglia FP (2009) Replay of rule-learning related neural patterns in the prefrontal cortex during sleep. Nature Neuroscience 12:919–926.

Siapas AG, Wilson MA (1998) Coordinated interactions between hippocampal ripples and cortical spindles during slow-wave sleep. Neuron 21:1123–1128.

Sirota A, Csicsvari J, Buhl D, Buzsáki G (2003) Communication between neocortex and hippocampus during sleep in rodents. Proc Natl Acad Sci USA 100:2065–2069.

Tauber WBW (1992) Clinical consequences of Thorotrast in a long-term survivor. Health Phys 63:13–19.

Wilson MA, McNaughton BL (1993) Dynamics of the hippocampal ensemble code for space. Science 261:1055–1058.

Ylinen A, Bragin A, Nádasdy Z, Jando G, Szabo I, Sik A, Buzsáki G (1995) Sharp wave-associated high-frequency oscillation (200 Hz) in the intact hippocampus: network and intracellular mechanisms. The Journal of Neuroscience 15:30–46.

Zhang K, Ginzburg I, McNaughton BL, Sejnowski TJ (1998) Interpreting neuronal population activity by reconstruction: unified framework with application to hippocampal place-cells. J Neurophysiol 79:1017–1044.

FIGURE LEGENDS

Figure 1. Bilateral connectivity diagram of the hippocampal circuit. The entorhinal cortex provides the major inputs into the hippocampus providing inputs to both Dentate Gyrus (DG) and CA1. Within the hippocampus information flows from DG to CA3, from CA3 to CA1 and then CA1 projects back to entorhinal cortex. These projections are largely ipsilateral, with the major exception being the subset of the Schaffer Collaterals that project to contralateral CA3 and CA1.

Figure 2. Sharp-ripples are generated simultaneously by the both hippocampi. The probability of detecting simultaneous sharp-wave ripples on two contra-lateral channels is the nearly equal to that for ipsi-lateral channels **A.** 500 ms of unfiltered hippocampal local field potential (LFP) recorded from dorsal CA1. The 500 ms segment contains several sharp-wave ripples. Ripples are detected by computing the envelope (ENV) of the band-pass (150-250 Hz) filtered signal (FILT). Peaks in the envelope that cross double threshold are defined as sharp-wave ripple events (RIP) **B.** 3 channels of LFP from each hemisphere recorded at the same time as **A.** Ripple detection was run on each channel independently and detected events are denoted as boxes behind the traces. **C.** Boxplots comparing the probability of detecting overlapping ripples on two different channels of LFP during run and sleep. **D.** Ripple peak triggered averages of unfiltered hippocampal LFP on three different channels. Averages were computed on the same channel as the trigger channel,

channels ipsilateral to the trigger channel, and channels contralateral to the trigger channel.

Figure 3. The amplitude and frequency of sharp-wave ripples are correlated both within and between the hippocampi. The phase of the ripple oscillations; however, is correlated within a hippocampus but not between the hippocampi. **A-B.** The joint distribution of mean ripple frequency for all coincident ipsilateral (A**)** and contralateral (B) ripple pairs. **C-D.** The distribution of ripple oscillation phase differences computed between ipsilateral (C) and contralateral (D) channels.

Figure 4. Hippocampal pyramidal cells increase their firing rate during sharp-wave ripples in the contra-lateral hippocampus. The increased spiking activity during sharp-wave ripples is correlated between the hippocampi and the normalized magnitude of bursts is correlated between hemispheres. **A.** An example of increased spiking activity in the right (RED) hippocampus during a ripple in the left (BLUE) hippocampus. **B.** Ripple triggered averages of the contralateral hippocampal multi-unit rate during run (RED) and sleep (BLUE). **C.** The bilateral cross-correlation of hippocampal multi-unit rate during peaks in the multi-unit firing for run (RED) and sleep (BLUE). **D.** The joint distribution of multi-unit firing rate, relative to the highest measured rate, for all multi-unit burst events.

Figure 5. Position estimates computed from spiking activity of each hippocampus are consistent during periods of navigation (velocity >15cm/sec). **A.** Posterior probability distributions of the decoded positions computed using the activity in a single hippocampus (a single lap, periods of immobility, is shown in greater detail). Darker shades of gray indicate higher probabilities. **B.** A confusion matrix constructed from the pdf modes restricted to time-bins when the animal was moving >15sm/sec. **C.** Boxplots demonstrating the precision of the confusion matrices computed for each data set. **D.** The distribution of correlations computed for each time-bin compared to a distribution of time shifted position estimates. **E.** Box plots of the mean correlation of decoded positions for each dataset.

Figure 6. Bayesian decoding of hippocampal activity reveals that the two hippocampi encode similar positions during candidate replay events. **A.** Examples of trajectories decoded from each hippocampus during PAUSE and SLEEP. **B.** The distribution of mean event correlations computed for events in a single compared to a null distribution for both PAUSE and SLEEP replay events. The null distribution was derived by shuffling events within the group of events of the same length. **C.** Box plots comparing the distributions mean correlation for all events vs. the null distribution in all data sets. **D.** The distribution of mean event correlations as a function of hippocampal multi unit firing rate for a single animal. **E.** Box plots showing the distribution across all animals of mean event correlations for events

high (>50% median) and low (<50% median) multi-unit firing rates during PAUSE and SLEEP.

FIGURES

FIGURE 1

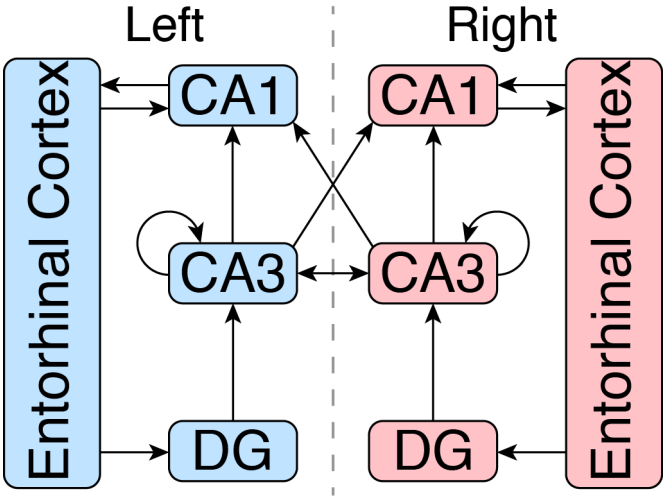
Left
Right
Entorhinal Cortex
CA1
CA1
CA3
CA3
DG
DG
Entorhinal Cortex

FIGURE 2

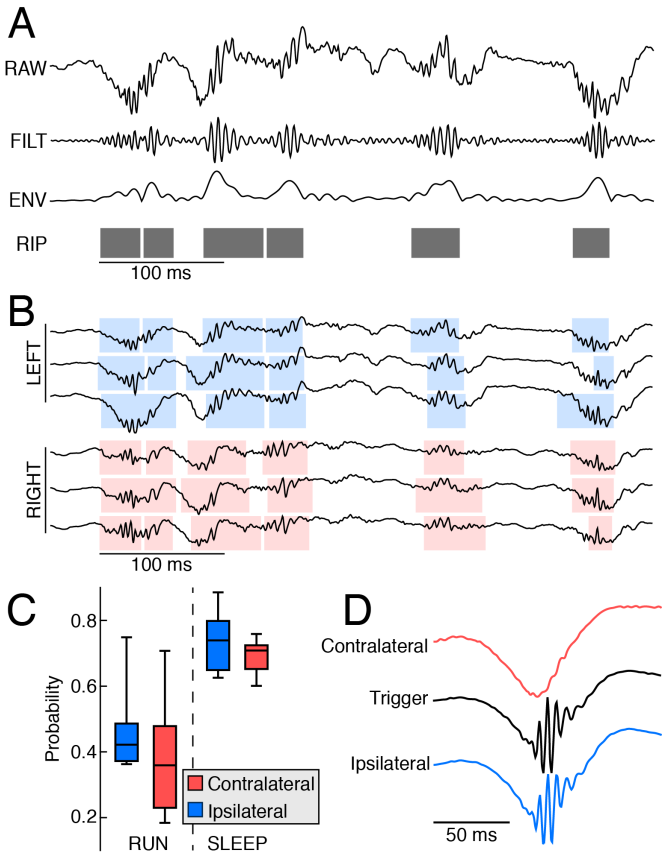
A
RAW
FILT
ENV
RIP
100 ms
B
LEFT
RIGHT
100 ms
C
Probability
0.8
0.6
0.4
0.2
Contralateral
Ipsilateral
RUN
SLEEP
D
Contralateral
Trigger
Ipsilateral
50 ms

FIGURE 3

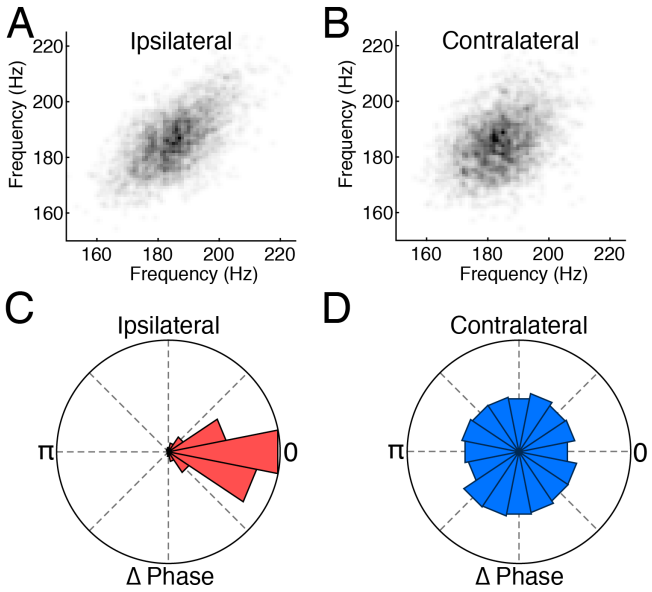

SW Amplitude Correlation

FIGURE 4

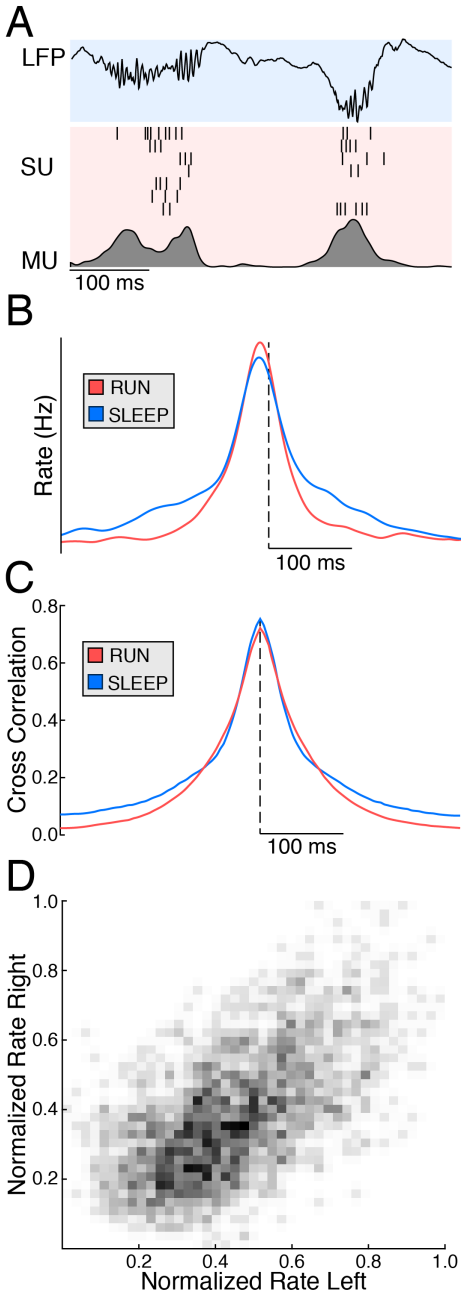
A
LFP
SU
MU
100 ms
B
RUN
SLEEP
Rate (Hz)
100 ms
C
RUN
SLEEP
Cross Correlation
0.0
0.2
0.4
0.6
0.8
100 ms
D
Normalized Rate Right
Normalized Rate Left
0.2
0.4
0.6
0.8
1.0

FIGURE 5

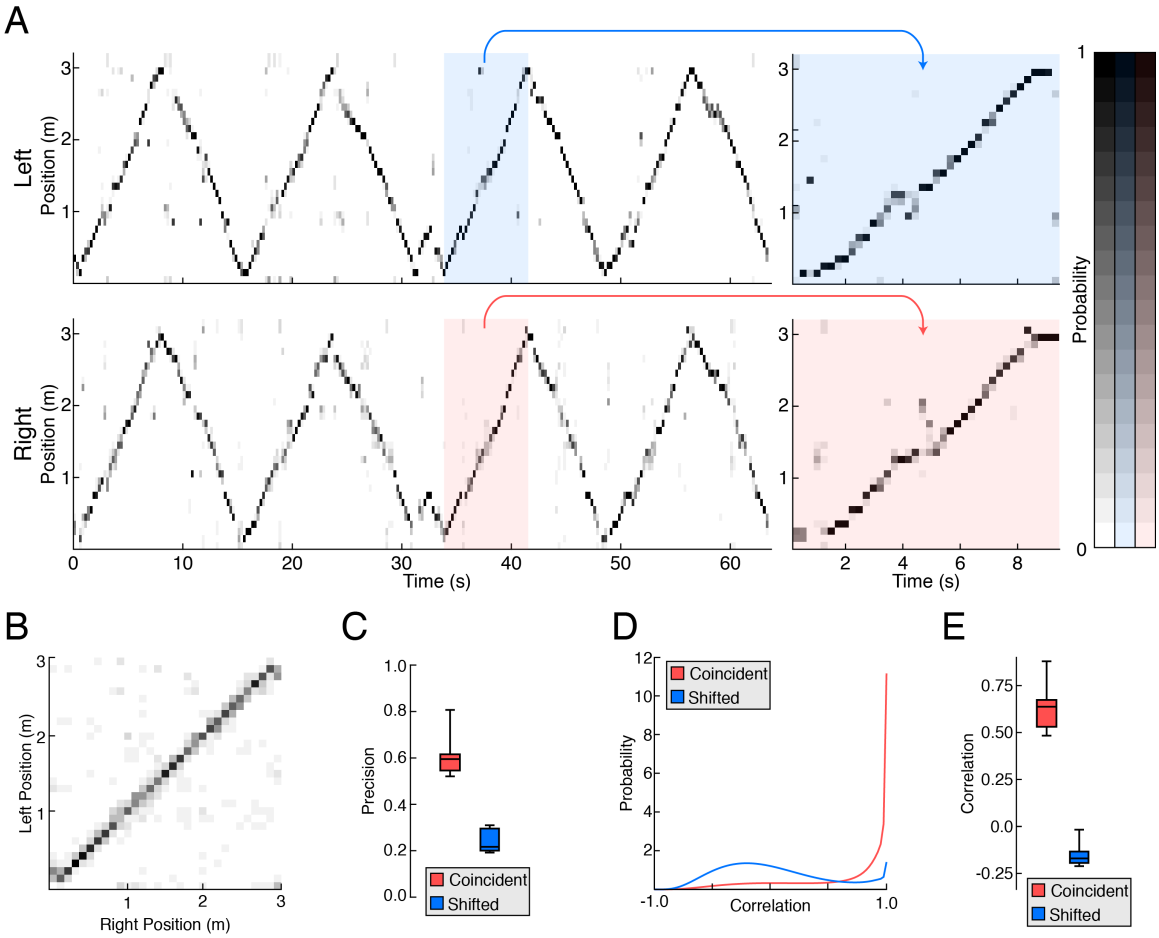
A
Left
Position (m)
Right
Position (m)
Time (s)
Time (s)
Probability
B
Left Position (m)
Right Position (m)
C
Precision
Coincident
Shifted
D
Coincident
Shifted
Probability
Correlation
E
Correlation
Coincident
Shifted

FIGURE 6

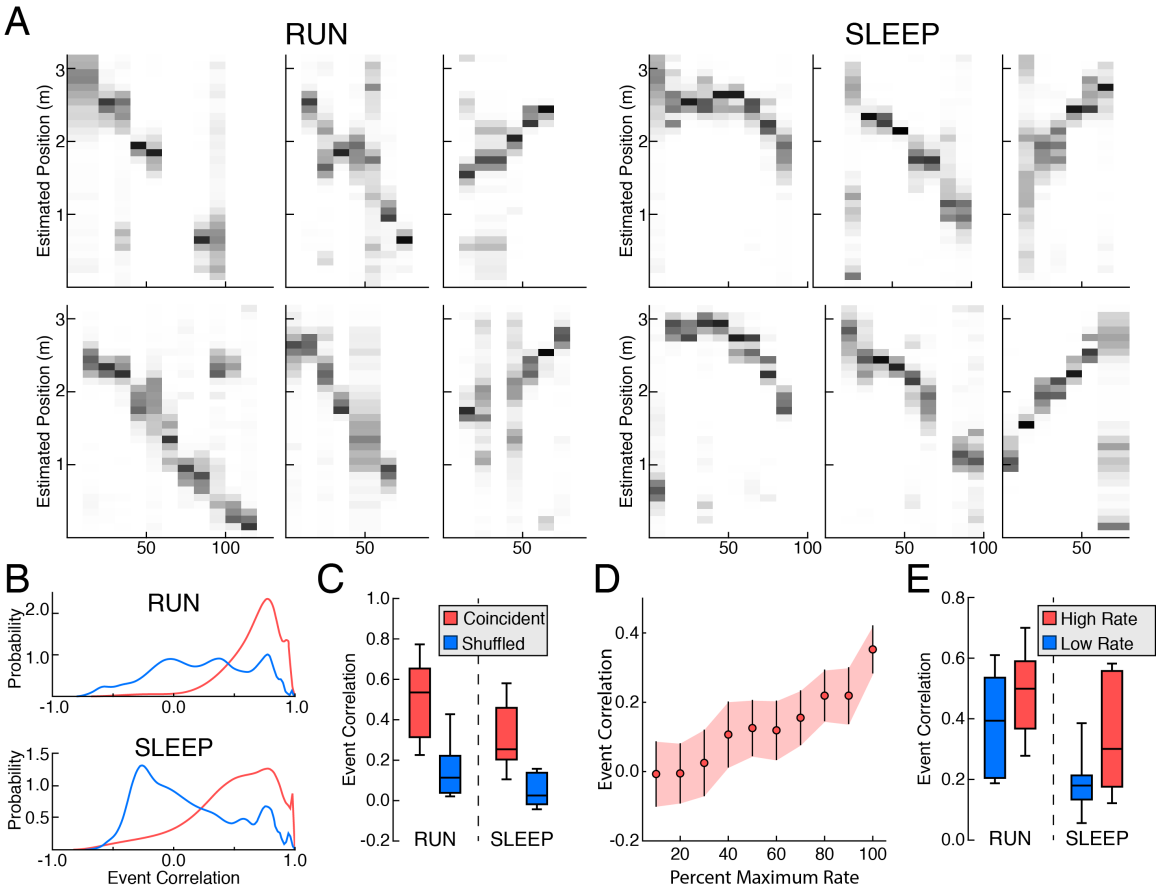
A
RUN
SLEEP
Estimated Position (m)
B
RUN
SLEEP
Probability
Event Correlation
C
Coincident
Shuffled
Event Correlation
RUN
SLEEP
D
Event Correlation
Percent Maximum Rate
E
High Rate
Low Rate
Event Correlation
RUN
SLEEP

The Temporal Structure of CA1 Ripple Events

INTRODUCTION

Uncovering the mechanisms of long-term memory formation has long been a pursuit of neuroscience; while a complete description of the mechanism is lacking, it is clear that the hippocampus plays an integral role. Lesion studies in both humans and animals have demonstrated that while the hippocampus does not store long-term memories (Squire & Alvarez, 1995), it is required for the formation of episodic memories (Schmolck, Kensinger, Corkin, & Squire, 2002). These findings demonstrated the importance in understanding the role of the hippocampus in determining the mechanisms of long-term memory formation. A prominent hypothesis of the hippocampus's role in memory formation suggests that during learning, novel and salient information is encoded by the hippocampus. Then during later off-line periods information temporarily stored in the hippocampus is transferred to cortex for long-term encoding(Buzsáki, 1989). Hippocampal replay(Lee & Wilson, 2002; Wilson & McNaughton, 1994) is a candidate mechanism for the transfer of information to cortex for long-term memory formation. Disruption of replay events during sleep and behavior negatively impacts the behavioral correlates of spatial learning (Ego-Stengel & Wilson, 2010; Girardeau, Benchenane, Wiener, Buzsáki, & Zugaro, 2009; Jadhav, Kemere, German, & Frank, 2012). Furthermore, hippocampal replay is temporally correlated with different types of activity in cortex, both at the level of the local-field potential and in unit activity (Ji & Wilson, 2007; Penagos, 2010; Peyrache, Khamassi, Benchenane, Wiener, &

Battaglia, 2009). These findings demonstrate that activity across the brain is correlated with hippocampal replay.

The global mechanisms responsible for coordinating what gets replayed and when are unknown. The timescales on which activity is coordinated are also unknown. Is replay coordinated at the levels of individual events or are events coordinated at some finer timescale? Coordination on the time-scale of sharp-wave ripples is likely since hippocampal unit activity is timed to ripples and replay events can span multiple ripples (Davidson, Kloosterman, & Wilson, 2009). Additionally individual ripples are correlated with spindles in cortex (Siapas & Wilson, 1998; Sirota, Csicsvari, Buhl, & Buzsáki, 2003).

This chapter will directly examine the temporal structure of ripple generation and present evidence that ripple generation is not random. Rather, evidence that ripple event generation is modulated by a 10-15 Hz rhythm is presented. We then observe this same rhythm in the unit activity of the hippocampus during ripple events, suggesting that the hippocampal replay code has rhythmic structure. Lastly, we will demonstrate the presence of similar rhythms the multi-unit activity of cortical regions downstream to the hippocampus. These results provide evidence that during potential replay events both hippocampal and cortical activity is coordinated to ripple events.

RESULTS

Timing of CA1 Ripples and Units

We analyzed the timing of ripple generation by the CA1 sub-region of the hippocampus. We started by detecting ripple events in the hippocampal LFP (**Figure 1A**) and then by grouping nearby ripples into sets. We then computed the intervals between adjacent ripple events (intervals greater than 1000ms were ignored, as they are not informative on the timescale of interest). The truncated distribution of inter-ripple-intervals was estimated using a histogram (5ms bins) and a kernel density estimator (**Figure 1B**). Both estimates had a peak at 75ms. The location of this peak indicates that ripple event generation is modulated by a 10-15 Hz rhythm. Additionally, we found that more than 25% of all ripple events are generated as members of a ripple set (**Figure 1C)**.

Next we examined if multi-unit activity (MUA) in CA1 reflects the rhythmicity observed in ripple generation. We thought it likely, as hippocampal unit activity increases during ripple events (**Figure 2A**). We then computed the average multi-unit firing rate in CA1 triggered on single ripples, doublets (sets with two or more ripples), and triplets (sets with three or more ripples). In all cases we observed a peak in the multi-unit firing rate that coincided with the ripple event. Furthermore, when doublets and triplets were used as the triggers, additional peaks were observed at 80 (**Figure 2B,C**) and 155ms (**Figure 2C**). The locations of these peaks

imply that unit activity in the hippocampus is modulated by the same 10-15 Hz rhythm that modulates ripple generation.

MUA in RSX is Correlated with HPC Ripple and MUA

We observed that MUA in RSX is moderately coordinated with ripples in CA1 (**Figure 3A**). To characterize the relationship between ripples in CA1 and unit activity in RSX, we computed the average RSX MUA triggered on single ripples and doublets (**Figure 3B**). We observed that, on average, the RSX MUA peaked 10ms prior to the ripple, decreased substantially during the ripple, and then recovered approximately 95ms following the ripple. When doublets were used as triggers the peak of the recovery was significantly greater than for single ripples. The timing observed in the ripple-triggered averages was also reflected in the cross-correlation of HPC and RSX multi-unit rates (**Figure 3C**).

Fast vs. Slow Doublets

Next we sought to determine if the frequency of ripple generation had an impact on the structure of MUA in CA1 and RSX. We classified doublets (sets with two or more ripples) as "fast" or "slow" using the mean inter-ripple-interval (IRI) for each doublet. Doublets with a mean IRI less than 75ms were classified as fast and all other doublets were classified as slow. We observed that, on average, the HPC MUA was synchronized to the individual ripples in the doublet, regardless of the doublet class (**Figure 4A**). However, the relationship between ripple timing and RSX MUA

is not as robust as CA1. As we observed previously, RSX MUA is suppressed at the state of both fast and slow doublets; however, in the case of fast doublets the RSX MUA was suppressed for the duration of the doublet. Conversely, when slow doublets were used as triggers RSX MUA recovered prior to the onset of the second ripple (**Figure 4B**). These results suggest that ripple set speed could serve as a gating mechanism that either facilitates or inhibits cross-structural coordination during replay events.

DISCUSSION

In summary we observed that timing of ripple generation by CA1 is modulated by a 10-15 Hz rhythm. Further evidence for this rhythm was also observed in the ripple associated MUA of CA1. Next, we demonstrated that unit activity in RSX is temporally correlated with CA1 ripples. Lastly we demonstrated that coordination between CA1 and RSX is stronger during slow ripple events. These results provide strong evidence that the 10-15Hz rhythm observed in HPC ripple and MUA activity likely exists in other structures.

Previous reports have demonstrated that hippocampal replay can span multiple ripples (Davidson et al., 2009). However, the dynamics governing the timing of ripple generation were undetermined. Furthermore, it was unknown whether ripples were generated with predictable timing or at random intervals. Here we have presented strong evidence that ripple generation is not random but rather event generation is modulated by a 10-15Hz rhythm. These results are important, as this structure will enable other brain regions to synchronize with replay-associated activity in the hippocampus. Future work should focus on identifying the source of this rhythm and connecting it to already classified oscillation such as sleep spindles and the beta rhythm.

Lastly, the finding that activity in RSX is entrained to slow doublets but not fast doublets suggest a dual function for HPC ripples. It may be that fast doublets are

expressed at times when the hippocampus is disconnected from its downstream structures and that slow doublets are used to facilitate the transfer of information between different brain regions.

METHODS

Electrophysiology and Behavior

Two male Long-Evans rats, weighing between 400 and 600 grams, were implanted with micro-drive arrays(Kloosterman et al., 2009) containing up to 30 independently movable tetrodes(Nguyen et al., 2009) targeted at dorsal CA1, retro-splenial cortex, and the anterior-dorsal thalamus. Following surgery, over the course of several weeks the tetrodes were slowly lowered into the brain until they reached their target structure. A single tetrode was left in white matter dorsal to CA1 to serve as a reference electrode. Signals from each tetrode were split into spike and local field potential channels. The spike channels were filtered between 300 Hz - 6 kHz. Extra-cellular action potentials were detected as threshold crossings on any tetrode channel, and a 32-sample spike waveform for each channel was recorded for each threshold crossing. Local field potential signals were filtered between 0.5 and 475 Hz and sampled at 1500 Hz. Data on tetrodes with noise was discarded.

Over the course of the experiment the rats were placed in a sleep box, or chamber used to encourage the sleeping. On several days the rats performed a navigation task, although only data acquired during sleep was analyzed. Movement in the sleep box was recorded using an overhead video camera and a precise estimate of position was computed using infrared light emitting diodes mounted on the micro-drive. Periods of prolonged immobility (>100 seconds) were analyzed. All

experiments were conducted in accordance with the guidelines of the US National Institute of Health, and under the supervision of their respective animal care facilities.

Ripple Event Detection

We used a variation of a previously published method to detect ripple events(Csicsvari et al., 1999) in the hippocampal local field potential. Briefly, the wide-band LFP was filtered between 150-250 Hz, and then the envelope of the filtered signal was computed using the absolute value of the Hilbert transform. Periods of time when the envelope of the filtered signal remained above a low threshold (1 SD) for at least 25ms while also exceeding a 2nd higher (5 SD) at least once were classified as candidate ripple events. Ripple times were computed as the timestamp of global maximum of the band-pass filtered signal for each event.

Ripple Set Classification

Ripple sets were constructed as follows. Any ripples that occurred more than 500ms after the previous ripple were assigned to a new set. All ripples that occurred within 250ms of the previous ripple were added to the previous ripple's set. Ripple sets containing a single ripple were classified as singlets while sets containing a minimum of 2 or 3 ripples were classified as doublets and triplets, respectively. Doublets were divided into fast and slow groups using the mean inter-ripple-interval for each set. Sets with a mean inter-ripple-interval less than 75ms were

classified as fast doublets; whereas, sets with a mean inter-ripple interval greater than 75ms were classified as slow doublets.

Multi-Unit Rate Estimates

The multi-unit firing rate for each structure was estimated using a variation of previously published methods(Davidson et al., 2009). Briefly, the multi-unit firing rate was estimated using a smoothed histogram (5ms bins; Gaussian kernel 10ms SD) constructed using the spike times from all tetrodes in the same structure, normalized by the number of tetrodes.

REFERENCES

Bendor, D., & Wilson, M. A. (2012). Biasing the content of hippocampal replay during sleep. Nature Neuroscience, 15(10), 1439–1444. doi:10.1038/nn.3203

Buzsáki, G. (1989). Two-stage model of memory trace formation: a role for "noisy" brain states. Neuroscience, 31(3), 551–570.

Csicsvari, J., Hirase, H., Czurkó, A., Mamiya, A., & Buzsáki, G. (1999). Fast network oscillations in the hippocampal CA1 region of the behaving rat. The Journal of Neuroscience : the Official Journal of the Society for Neuroscience, 19(16), RC20.

Davidson, T. J., Kloosterman, F., & Wilson, M. A. (2009). Hippocampal replay of extended experience. Neuron, 63(4), 497–507. doi:10.1016/j.neuron.2009.07.027

Diba, K., & Buzsáki, G. (2007). Forward and reverse hippocampal place-cell sequences during ripples. Nature Neuroscience, 10(10), 1241–1242. doi:10.1038/nn1961

Ego-Stengel, V., & Wilson, M. A. (2010). Disruption of ripple-associated hippocampal activity during rest impairs spatial learning in the rat. Hippocampus, 20(1), 1–10. doi:10.1002/hipo.20707

Foster, D. J., & Wilson, M. A. (2007). Hippocampal theta sequences. Hippocampus, 17(11), 1093–1099. doi:10.1002/hipo.20345

Girardeau, G., Benchenane, K., Wiener, S. I., Buzsáki, G., & Zugaro, M. B. (2009). Selective suppression of hippocampal ripples impairs spatial memory. Nature Neuroscience, 12(10), 1222–1223. doi:10.1038/nn.2384

Jadhav, S. P., Kemere, C., German, P. W., & Frank, L. M. (2012). Awake hippocampal sharp-wave ripples support spatial memory. Science, 336(6087), 1454–1458. doi:10.1126/science.1217230

Ji, D., & Wilson, M. (2007). Coordinated memory replay in the visual cortex and hippocampus during sleep. Nature Neuroscience, 10(1), 100–107. doi:10.1038/nn1825

Kloosterman, F., Davidson, T. J., Gomperts, S. N., Layton, S. P., Hale, G., Nguyen, D. P., & Wilson, M. A. (2009). Micro-drive array for chronic in vivo recording: drive fabrication. Journal of Visualized Experiments, (0). doi:10.3791/1094

Lee, A. K., & Wilson, M. A. (2002). Memory of sequential experience in the hippocampus during slow wave sleep. Neuron, 36(6), 1183–1194.

Logothetis, N. K., Eschenko, O., Murayama, Y., Augath, M., Steudel, T., Evrard, H. C., et al. (2012). Hippocampal-cortical interaction during periods of subcortical silence. Nature, 491(7425), 547–553. doi:10.1038/nature11618

Mölle, M., Yeshenko, O., Marshall, L., Sara, S. J., & Born, J. (2006). Hippocampal sharp wave-ripples linked to slow oscillations in rat slow-wave sleep. Journal of Neurophysiology, 96(1), 62–70. doi:10.1152/jn.00014.2006

Nguyen, D. P., Layton, S. P., Hale, G., Gomperts, S. N., Davidson, T. J., Kloosterman, F., & Wilson, M. A. (2009). Micro-drive array for chronic in vivo recording: tetrode assembly. Journal of Visualized Experiments, (26). doi:10.3791/1098

Penagos, H. (2010, June 10). Interactions Between Anterior Thalamus and Hippocampus during Different Behavioral States in the Rat

. Massachusetts Institute of Technology, Cambridge, MA.

Peyrache, A., Khamassi, M., Benchenane, K., Wiener, S. I., & Battaglia, F. P. (2009). Replay of rule-learning related neural patterns in the prefrontal cortex during sleep. Nature Neuroscience, 12(7), 919–926. doi:10.1038/nn.2337

Schmolck, H., Kensinger, E. A., Corkin, S., & Squire, L. R. (2002). Semantic knowledge in patient H.M. and other patients with bilateral medial and lateral temporal lobe lesions. Hippocampus, 12(4), 520–533. doi:10.1002/hipo.10039

Siapas, A. G., & Wilson, M. A. (1998). Coordinated interactions between hippocampal ripples and cortical spindles during slow-wave sleep. Neuron, 21(5), 1123–1128.

Sirota, A., Csicsvari, J., Buhl, D., & Buzsáki, G. (2003). Communication between neocortex and hippocampus during sleep in rodents. Proceedings of the National Academy of Sciences of the United States of America, 100(4), 2065–2069. doi:10.1073/pnas.0437938100

Squire, L. R., & Alvarez, P. (1995). Retrograde amnesia and memory consolidation: a neurobiological perspective. Current Opinion in Neurobiology, 5(2), 169–177.

Wilson, M. A., & McNaughton, B. L. (1994). Reactivation of hippocampal ensemble memories during sleep. Science.

FIGURE LEGENDS

Figure 1. Ripple generation by CA1 is modulated by a 10-15 Hz rhythm. **A.** 4 examples of unfiltered local field potential, recorded in CA1. Each trace contains a set of sharp-wave ripple events. **B.** The distribution of inter-ripple-intervals was estimated using an unsmoothed histogram (5ms time-bins) and a kernel density estimator. **C.** The distribution of ripple set size, truncated to a set length of 5.

Figure 2. During ripple sets, CA1 unit activity is entrained by the same rhythm that modulates the timing of ripple generation. **A.** 3 examples of unfiltered local field potential and the multi-unit firing rate, both in CA1, during ripple sets. **B.** The average multi-unit firing rate in CA1 triggered on all ripples (black), single ripples (red), and ripple doublets (blue), sets with 2 or more ripples. **C.** The average multi-unit firing rate in CA1 triggered on all ripples (black), single ripples (red), and ripple triplets (green), sets with 3 or more ripples.

Figure 3. During ripple sets, unit activity in RSX is correlated with both unit and ripple activity in CA1. **A.** 3 examples of unfiltered local field potential, in CA1, and the multi-unit firing rate in RSX. **B.** The average multi-unit firing rate in RSX triggered on single ripples (red) and ripple doublets (blue). **C.** The cross correlation of the multi-unit firing from CA1 and RSX.

Figure 4. Unit activity in RSX is more strongly modulated by slow ripple sets (mean inter-ripple-interval > 75ms) than fast ripple sets (mean inter-ripple-interval < 75ms). **A.** The average multi-unit firing rate in HPC triggered on fast (blue) and slow (gray) ripple doublets. **B.** The average multi-unit firing rate in RSX triggered on fast (green) and slow (gray) ripple doublets.

FIGURES

Figure 1

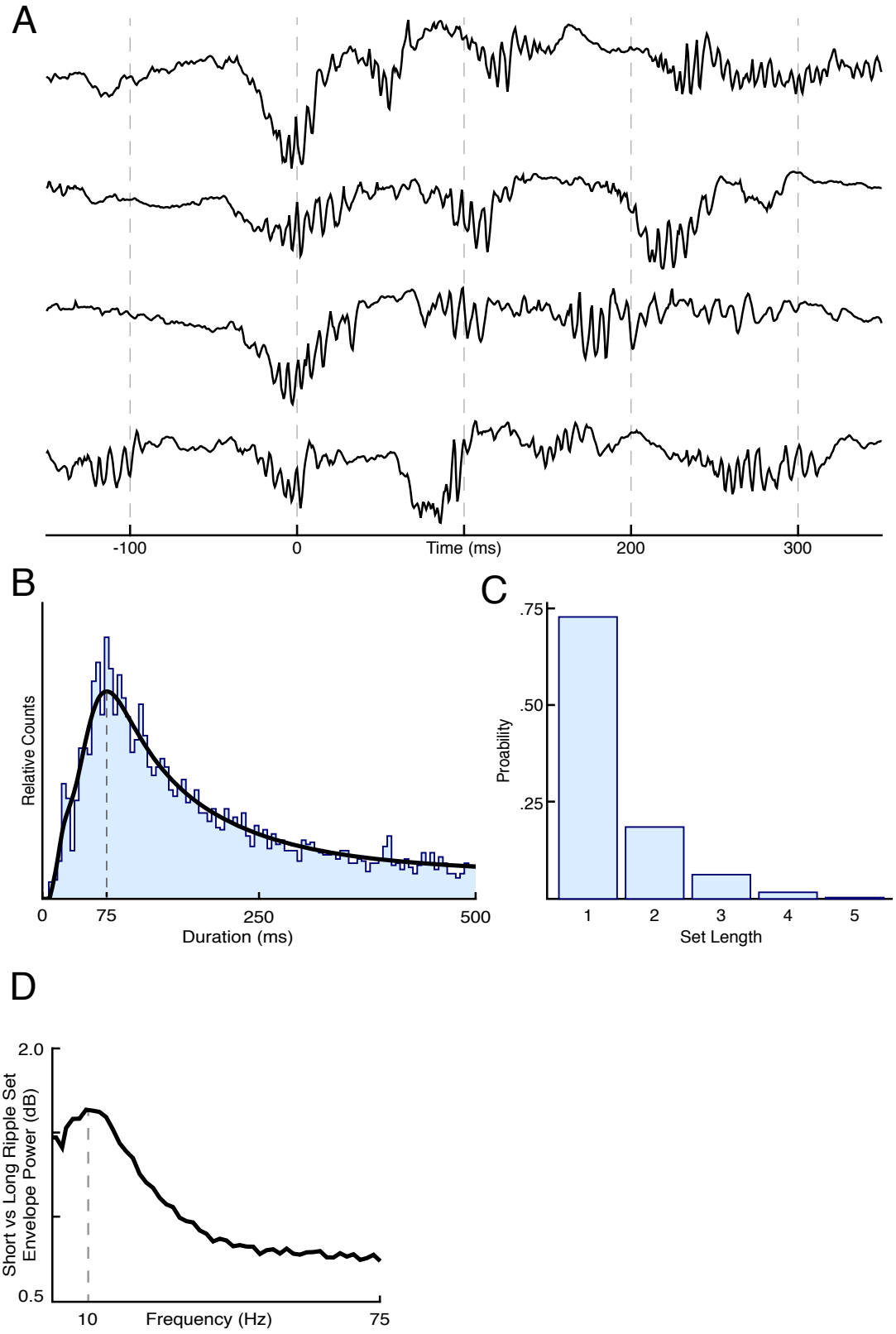
A
-100
0
Time (ms)
200
300
B
Relative Counts
0
75
250
500
Duration (ms)
C
.75
.50
.25
Proability
1
2
3
4
5
Set Length
D
2.0
0.5
Short vs Long Ripple Set
Envelope Power (dB)
10
Frequency (Hz)
75

Figure 2

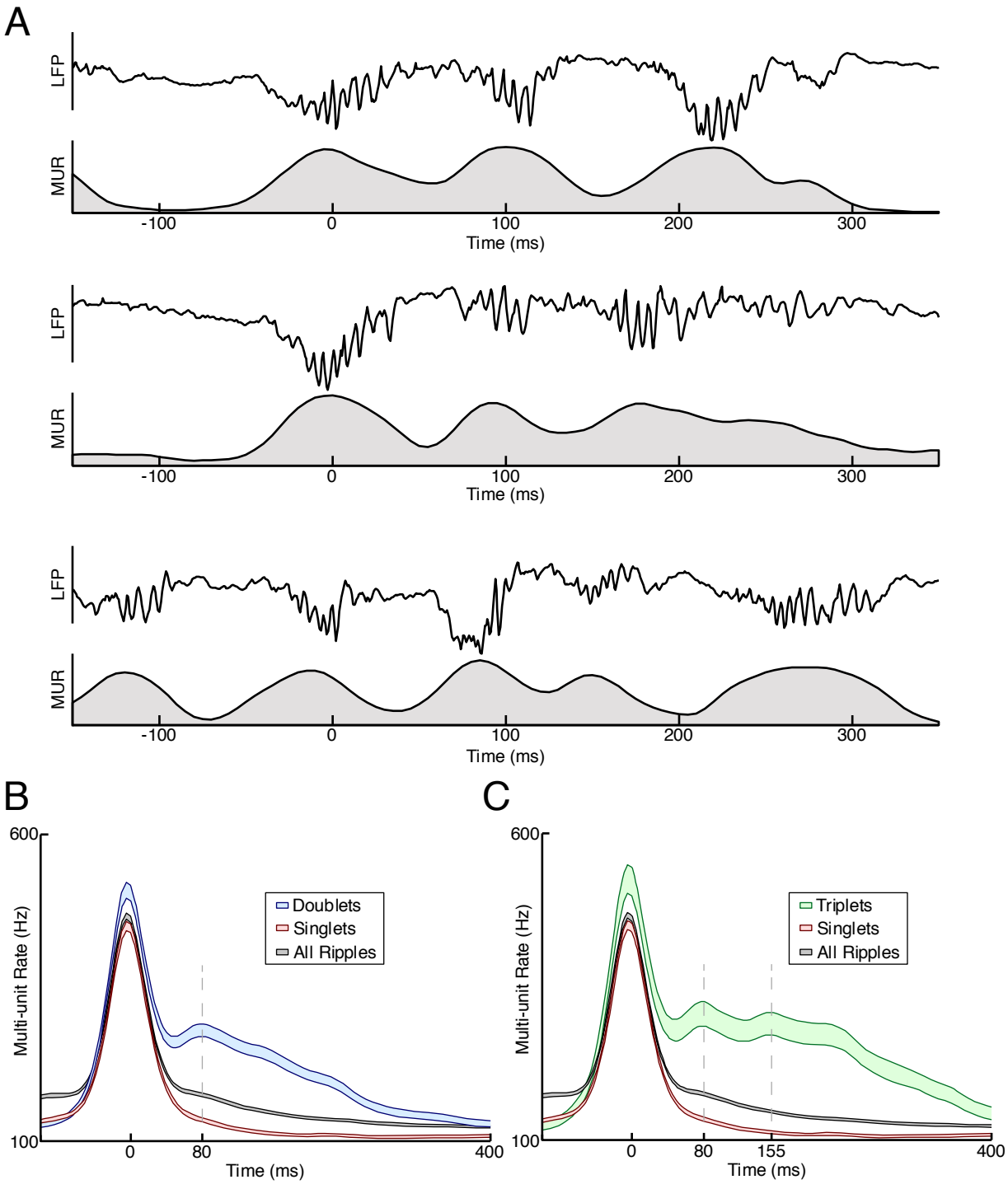
A
LFP
MUR
-100
0
100
200
300
Time (ms)
B
C
600
100
Multi-unit Rate (Hz)
Doublets
Singlets
All Ripples
Triplets
0
80
155
400
Time (ms)

Figure 3

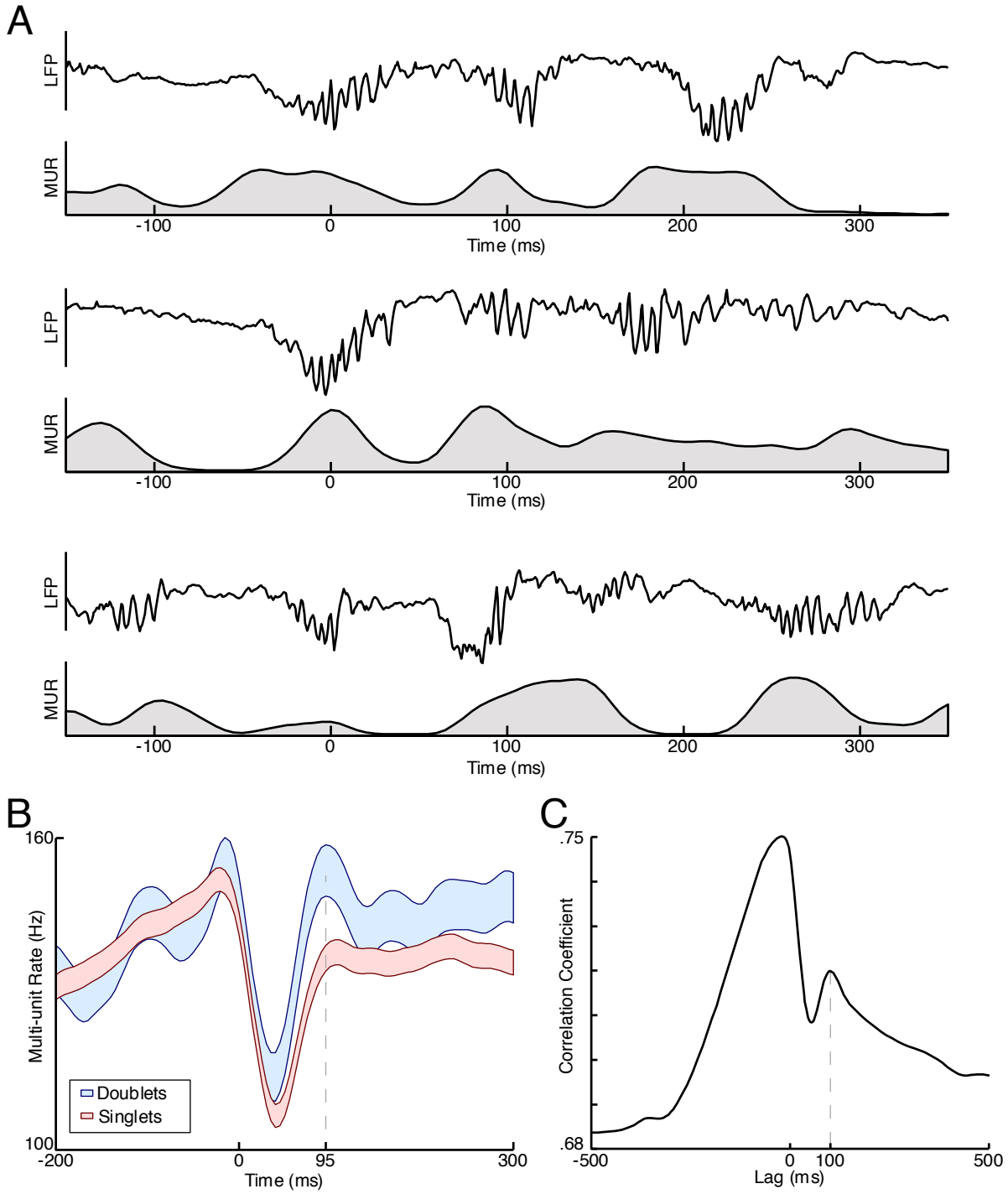
A
LFP
MUR
-100
0
100
200
300
Time (ms)
LFP
MUR
-100
0
100
200
300
Time (ms)
LFP
MUR
-100
0
100
200
300
Time (ms)
B
160
100
Multi-unit Rate (Hz)
Doublets
Singlets
-200
0
95
300
Time (ms)
C
.75
.68
Correlation Coefficient
-500
0
100
500
Lag (ms)

Figure 4

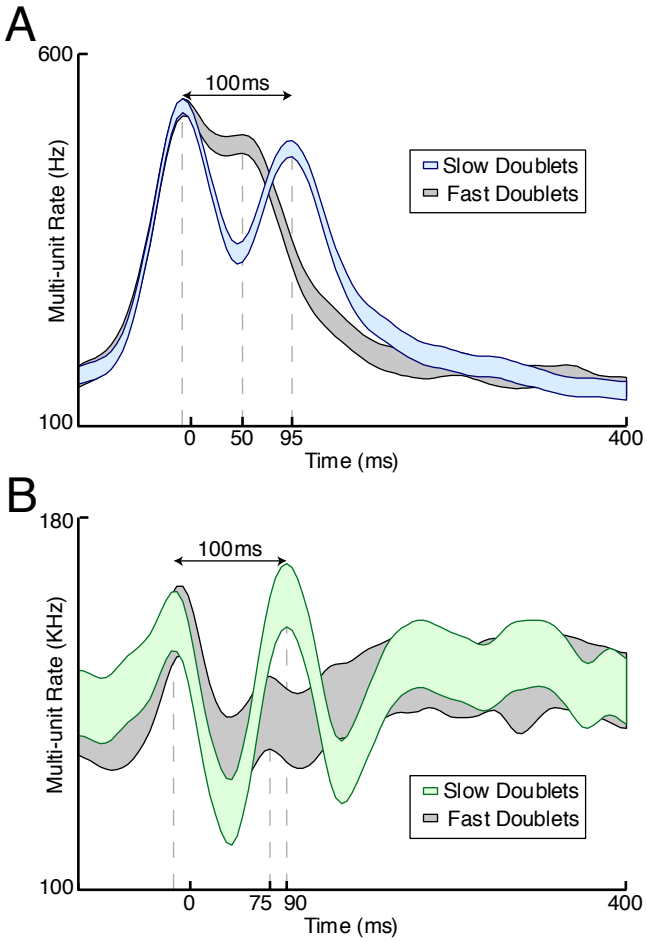
A
600
100
100ms
Multi-unit Rate (Hz)
Slow Doublets
Fast Doublets
0
50
95
400
Time (ms)
B
180
100
100ms
Multi-unit Rate (KHz)
Slow Doublets
Fast Doublets
0
75
90
400
Time (ms)

Bayesian Decoding of Unsorted Spike-Trains

This chapter is currently under review with the Journal of Neurophysiology: JN-01046-2012 Bayesian Decoding using Unsorted Spikes in the Rat Hippocampus, F. Kloosterman, S. Layton, Z. Chen, M. Wilson *(under review)*

Abstract

A fundamental task in neuroscience is to understand how neural ensembles represent information. Population decoding is a useful tool to extract information from neuronal populations based on the ensemble spiking activity. We propose a novel Bayesian decoding paradigm to decode unsorted spikes in the rat hippocampus. By directly using spike waveform features such as the peak amplitude, our approach integrates encoding and decoding into a coherent framework and avoids accumulation of spike-sorting errors. Our decoding paradigm is nonparametric, encoding model-free for representing stimuli, and minimizes information loss by utilizing all available spikes. We apply the proposed Bayesian decoding algorithm to a position reconstruction task for freely behaving rats based on tetrode recordings of rat hippocampal neuronal activity. Our detailed decoding analyses demonstrate that our approach is efficient and provides a more accurate position estimate than the standard sorting-based decoding algorithm. Our approach can be adapted to an online encoding/decoding framework for applications that require real-time decoding, such as brain-machine interfaces.

INTRODUCTION

Features of sensory stimuli and intended motor actions are reflected in the activity of neuronal ensembles that are distributed across the brain (Sanger, 2003; Huys et al., 2007; Boloori et al., 2010). A fundamental goal in neuroscience is to understand how the information about external stimuli is transformed into neural activity patterns and how this information is represented in the brain. The relationship between stimuli and neural activity can be described by statistical encoding models (Brown et al., 1998; Sanger, 2003; Truccolo et al., 2005; Paninski et al., 2007). Inversion of these encoding models, i.e. extraction of information about the stimulus from observed neural activity ("neural decoding"), aids in revealing the principles of the encoding process (Quian Quiroga and Panzeri, 2009). Neural decoding can also be applied to uncover internal neural representations in the absence of an overt stimulus, for example the re-expression of spatial sequences in the hippocampus (Davidson et al., 2009; Gupta et al., 2010) or movement intentions in motor cortices (Georgopoulos et al., 1986; Zhuang et al., 2010). Decoding motor plans in particular is an important part of the development of neural prosthetics and brain-machine interfaces which may restore motor function in patients with neurological damage (Chapin, 2004; Schwartz et al., 2006; Hochberg et al., 2012).

The principal goal of neural decoding is to extract as much information about a stimulus as possible from a neural signal. As with all signal processing, any additional operation on the raw signal in neural decoding adds complexity and leads

to possible loss of information. Most approaches for decoding neural spiking activity rely on the intermediate step of sorting spike waveforms into groups of single units. The spike sorting process is subject to at least two problems that could affect decoding performance. The first issue is that the goal of neural decoding to minimize the decoding error is substantially different from the goal to label each spike uniquely and confidently with the identity of the cell that emitted it. In particular spike sorting is generally conservative and many spikes are left unclassified in an attempt to minimize classification errors. However, spikes thrown out during the sorting process could still convey information about the stimulus and hence contribute to decoding performance. Second, inherent to spike sorting are misclassification errors – that is, incorrect assignment of spikes to a unit. Theoretical analysis has shown that different spike sorting errors have various impacts on information capacity, with false positive errors having the most serious effect (Goodman and Johnson, 2008). Another potential source of misclassification is the use of hard decision boundaries – it has been suggested that a soft decision boundary is more appropriate for evaluating neural ensemble codes (Wood and Black, 2008).

To maximize the stimulus information extracted from neural spiking activity, we propose a novel Bayesian decoding paradigm that does not require the intermediate step of spike sorting. Key in our approach is a direct mapping between the raw data (i.e. spike waveform features) and the stimulus in a joint probability distribution.

This allows all detected spikes to be incorporated into the decoding process and hence information loss is minimized. In contrast to previous work, our approach does not assume a parametric or biophysical model to describe the relation between stimulus and neural activity.

The performance of the new decoding approach is analyzed by applying it to hippocampal population recordings in order to estimation the location of a rat on a track.

METHODS

Spike feature decoding framework

ENCODING MODEL. The ultimate goal of our method is to reconstruct a sensory stimulus, motor action or other covariate (from here on referred to as "stimulus") from neuronal spiking activity recorded from an array of sensors (e.g. single wire electrodes, stereotrodes or tetrodes). First, we build an encoding model that relates the neural activity on a single sensor to the stimulus of interest. Let's assume that in the time period $(0, T]$ we recorded the time varying stimulus vector $\boldsymbol{x}(t)$ as well as N discrete spike events and their waveforms at times t_n, with $0 < t_1 < t_2 < \cdots < t_N \leq T$. The detected spikes are treated as a spatial-temporal Poisson process, or equivalently as a marked temporal Poisson process, in which the spatial component (the "mark") is a vector space S of spike waveform features $\boldsymbol{a} \in S$. Examples of typical waveform features are peak amplitude, spike width, extracted principal components or other derived features. The same waveform features are generally used by spike sorting processes to extract single units from multi-unit activity. In our approach the spike-sorting step is bypassed by creating a direct mapping between spike waveform features and stimulus (Fig. 1). The spatial-temporal Poisson process is fully characterized by its generalized rate function $\lambda(\boldsymbol{a}, t)$. In cases when the rate is determined by the stimulus of interest, the rate function can be re-expressed as $\lambda(\boldsymbol{a}, t) = \lambda(\boldsymbol{a}, \boldsymbol{x}(t))$. Here, $\lambda(\boldsymbol{a}, \boldsymbol{x})$ can be viewed as a tuning curve which relates the average rate of spike events with waveform features $\boldsymbol{a}$ to the stimulus $\boldsymbol{x}$.

To compute the probability that we observe n spikes with associated features $\boldsymbol{a}_{1:n}$ in a small time window $[t, t+\Delta t)$ in the presence of a known stimulus, the waveform feature space S is first divided into J non-overlapping regions: $S \equiv \left(S_1 \cup S_2 \cup \cdots \cup S_J\right)$. Each region S_j contains n_j spikes, which is a subset of the observed n spikes (i.e. $\sum_{j=1}^{J} n_j = n$). The expected number of spikes in each region S_j follows a Poisson distribution with rate function: $\lambda_{S_j}(\boldsymbol{x}) = \int_{S_j} \lambda(\boldsymbol{a}, \boldsymbol{x}) d\boldsymbol{a}$. The likelihood of finding exactly $n_{1:J}$ spikes in regions $S_{1:J}$ can be computed from the product of Poisson likelihoods of all regions:

$$P(\boldsymbol{a}_{1:n}|\boldsymbol{x}) = P\left(n_{1:J}\middle|\boldsymbol{x}\right) = \prod_{j=1}^{J} P\left(n_j\middle|\boldsymbol{x}\right) = \prod_{j=1}^{J} Poisson\left(n_j; \lambda_{S_j}(\boldsymbol{x})\right)$$
$$= \frac{\left[\prod_{j=1}^{J}\left(\Delta t \int_{S_j} \lambda(\boldsymbol{a}, \boldsymbol{x}) d\boldsymbol{a}\right)^{n_j}\right]\left[e^{-\Delta t \sum_{j=1}^{J} \int_{S_j} \lambda(\boldsymbol{a}, \boldsymbol{x}) d\boldsymbol{a}}\right]}{\prod_{j=1}^{J} n_j!} \quad (1)$$

In the limiting case when regions $S_{1:J}$ become sufficiently small such that $n_{1:J}$ are equal to 0 or 1 within the time interval Δt, the likelihood can be rewritten as:

$$P(\boldsymbol{a}_{1:n}|\boldsymbol{x}) = (\Delta t)^n \left[\prod_{i=1}^{n} \lambda(\boldsymbol{a}_i, \boldsymbol{x})\right]\left[e^{-\Delta t \lambda(x)}\right] \quad (2)$$

This likelihood function, when calculated for all possible waveform feature vectors $\boldsymbol{a}$, completely characterizes the encoding process for a single sensor. For multiple sensors, assuming conditional spiking independence between sensors (i.e., each sensor records from an independent population of neurons), the joint data likelihood can be computed as a product of individual likelihoods contributed by each sensor.

For K sensors and n_k spike events on the k-th electrode, the joint likelihood is given by:

$$P(\boldsymbol{a}^{1:K}|\boldsymbol{x}) = \prod_{k=1}^{K} P(\boldsymbol{a}_{1:n_k}|\boldsymbol{x}) \tag{3}$$

RELATION TO ENCODING WITH SPIKE SORTED UNITS. It is possible to choose the spike feature $\boldsymbol{a}$ such that it is a discrete scalar variable that represents cell identity (for example obtained through a spike sorting procedure). In that case, each region S_j can be constructed such that it corresponds to a single cell c. This means that $\lambda_c(x) = \lambda_{S_j}(x)$ is the tuning curve of cell c and $n_c = n_j$ is the number of spikes emitted by cell c. By rewriting Eq. (1) we recover the likelihood for a population of spike sorted cells as a special case (Zhang et al., 1998):

$$P(n_{1:C}|\boldsymbol{x}) = \left[\frac{(\Delta t)^N}{\prod_{i=1}^{C} n_i!}\right]\left[\prod_{c=1}^{C} \lambda_c(\boldsymbol{x})^{n_c}\right]\left[e^{-\Delta t \sum_{c=1}^{C} \lambda_c(\boldsymbol{x})}\right] \tag{4}$$

where C is the total number of cells and $N = \sum_{c=1}^{C} n_c$ is the total number of spike events.

EVALUATION OF THE LIKELIHOOD. To compute the likelihood in Eq. (2), representations of the generalized rate function $\lambda(\boldsymbol{a}, \boldsymbol{x})$ and its marginal rate function $\lambda(\boldsymbol{x})$ need to be constructed. A parametric model of the rate functions would allow for straightforward evaluation during decoding, however, it is not clear what model, if any, would be appropriate. In contrast, non-parametric models

provide a more flexible estimate of the rate functions. For low dimensional problems simple histogram based rate functions can be pre-computed. This approach, however, quickly becomes impractical for a higher number of dimensions. For instance, tetrode recordings have four feature dimensions (e.g. spike waveform peak amplitude on each of the four tetrode wires) and at least one stimulus dimension. If each dimension were divided into 100 bins, a histogram-based representation would require a minimum of 100^5 or 10,000,000,000 elements to be stored. This representation would require over 18 GB of memory (assuming 2 bytes of memory per element) for each tetrode and over 300 GB for an array of 18 tetrodes. In practice this representation would be extremely wasteful as only a fraction of the elements will be non-zero. For this reason we used kernel-density based estimators of the rate functions that are evaluated during the decoding process (see Bayesian decoding).

To construct the kernel-density estimators, the generalized rate function $\lambda(\boldsymbol{a}, \boldsymbol{x})$ and the marginal rate function $\lambda(\boldsymbol{x})$ are decomposed into spike event probability distributions ($p(\boldsymbol{a}, \boldsymbol{x})$ and $p(\boldsymbol{x})$) and a stimulus probability distribution ($\pi(\boldsymbol{x})$):

$$\lambda(\boldsymbol{a}, \boldsymbol{x}) = \frac{\#spikes(\boldsymbol{a}, \boldsymbol{x})}{occupancy(\boldsymbol{x})} = \frac{N}{T}\frac{p(\boldsymbol{a}, \boldsymbol{x})}{\pi(\boldsymbol{x})} = \mu\frac{p(\boldsymbol{a}, \boldsymbol{x})}{\pi(\boldsymbol{x})} \tag{5}$$

$$\lambda(\boldsymbol{x}) = \mu\frac{p(\boldsymbol{x})}{\pi(\boldsymbol{x})} \tag{6}$$

Here, *#spikes* represents a spike count, *occupancy* represents the total presentation time of stimulus $\boldsymbol{x}$; N is the total number of spikes recorded in the time interval $(0, T]$ and μ is the average spiking rate.

The probability distributions $p(\boldsymbol{a}, \boldsymbol{x})$, $p(\boldsymbol{x})$ and $\pi(\boldsymbol{x})$ can be estimated using the following multivariate kernel product density estimators:

$$p(\boldsymbol{a}, \boldsymbol{x}) = \frac{1}{N} \sum_{n=1}^{N} \prod_{i=1}^{d} K_{h_i}(\boldsymbol{a} - \tilde{\boldsymbol{a}}_{i,n}) \prod_{j=1}^{q} K_{h_j}(\boldsymbol{x} - \tilde{\boldsymbol{x}}_{j,n}) \tag{7}$$

$$p(\boldsymbol{x}) = \frac{1}{N} \sum_{n=1}^{N} \prod_{j=1}^{q} K_{h_j}(\boldsymbol{x} - \tilde{\boldsymbol{x}}_{j,n}) \tag{8}$$

$$\pi(\boldsymbol{x}) = \frac{1}{R} \sum_{r=1}^{R} \prod_{j=1}^{q} K_{h_j}(\boldsymbol{x} - \tilde{\boldsymbol{x}}_{j,r}) \tag{9}$$

Here, d is the dimensionality of the feature vector $\boldsymbol{a}$ and q is the dimensionality of the stimulus $\boldsymbol{x}$. $\{\tilde{\boldsymbol{a}}_n, \tilde{\boldsymbol{x}}_n\}_{n=1}^{N}$ represents the set of N spikes with associated feature vectors and stimuli which are collected during the encoding phase. $\{\tilde{\boldsymbol{x}}_r\}_{r=1}^{R}$ represents the set of R observed (or chosen) stimuli, which are generally sampled at regular time intervals during the encoding stage. $K_h(\cdot)$ is a kernel function with bandwidth h. Examples of kernels that may be used are: Gaussian, Epanechnikov, uniform, von Mises (for circular variables) or Kronecker delta (for discrete variables). The bandwidth of a kernel determines the amount of smoothing that is applied to the underlying data and therefore has a strong influence on the shape of the final density estimate.

BAYESIAN DECODING. To infer the uncertainty or probability of a hidden stimulus $\boldsymbol{x}_t$ at time t given the observed m spike events with associated features $\boldsymbol{a}_{1:m}$, we resort to Bayes rule:

$$P(\boldsymbol{x}_t|\boldsymbol{a}_{1:m}) = \frac{P(\boldsymbol{a}_{1:m}|\boldsymbol{x}_t)P(\boldsymbol{x}_t)}{P(\boldsymbol{a}_{1:m})} \tag{10}$$

Bayes rule provides a way to combine prior information about the stimulus $P(\boldsymbol{x}_t)$ with information obtained from observations through the likelihood function $P(\boldsymbol{a}_{1:m}|\boldsymbol{x}_t)$ (taken from Eqs. (2) and (3)). The denominator $P(\boldsymbol{a}_{1:m})$ is a normalizing constant such that the posterior $P(\boldsymbol{x}_t|\boldsymbol{a}_{1:m})$ is a proper probability distribution. The posterior distribution contains all information about the stimulus at time t that can be extracted from the observed spike events. If a non-informative temporal prior is assumed, then the aim of Bayesian decoding is to maximize the product of the likelihood and time-independent prior: $P(\boldsymbol{x}|\boldsymbol{a}_{1:m}) \propto P(\boldsymbol{a}_{1:m}|\boldsymbol{x})P(\boldsymbol{x})$. If a completely non-informative prior is assumed, then Bayesian decoding is analogous to maximum likelihood estimation: $P(\boldsymbol{x}|\boldsymbol{a}_{1:m}) \propto P(\boldsymbol{a}_{1:m}|\boldsymbol{x})$.

IMPLEMENTATION. The spike feature based decoder was implemented in Matlab (The Mathworks, Natick, MA) with custom C extensions. In Eqs. (5)-(9) we developed a representation for the rate functions $\lambda(\boldsymbol{a},\boldsymbol{x})$ and $\lambda(\boldsymbol{x})$, which are needed to compute the likelihood in Eq. (2). These rate functions are evaluated during the decoding stage and hence the only operation performed during encoding is the storage of the detected spikes and the stimulus. Decoding is performed separately for pre-defined time bins. For each detected spike and its associated features within a time bin, the rate function $\lambda(\boldsymbol{a},\boldsymbol{x})$ (Eq. (5)) is evaluated at a user-defined grid in stimulus space. Note that $p(\boldsymbol{x})$ and $\pi(\boldsymbol{x})$ and hence $\lambda(\boldsymbol{x})$ can be pre-computed as they only depend on the spikes recorded in the encoding stage and not on the spikes observed in the

decoding stage. Finally, the likelihood (Eqs. (2) and (3)) and the posterior distributions (Eq. (10)) can be computed. Computations are performed in log-space, such that products in Eq. (2) are replaced by summations.

Application to hippocampal recordings

ELECTROPHYSIOLOGY AND BEHAVIOR. Eight male Long-Evans rats, weighing between 400 and 600 grams, were implanted with custom-made micro-drive arrays (Kloosterman et al., 2009; Nguyen et al., 2009). Individual arrays carried between 9-24 independently moveable tetrodes targeted to either the right dorsal hippocampus (n=8) or bilaterally to both hippocampi (n=4) (coordinates: 2.5 mm lateral and 4.0 mm posterior to bregma). The tetrodes were slowly lowered into the brain until they reached the cell layer of CA1 two to four weeks following array implantation. A reference electrode was positioned in the white matter overlying the dorsal hippocampus. In the case of bilateral recordings, separate ipsilateral references were used for each hippocampus. Signals were filtered between 300 Hz - 6 kHz and all extracellular spike waveforms that crossed a preset amplitude threshold (73uV) on any of the four tetrode channels were sampled at 31250 Hz (32 samples per spike waveform) and saved to disk.

During 30-60 minute long recording sessions rats were allowed to freely explore a 3.1-m linear track. While no behavioral restrictions were placed on the rats, they did receive a small food reward (chocolate sprinkle, fruit loop, etc.) at alternating ends of the track to encourage exploration. The position of the rats was tracked at

30 Hz using an overhead video camera and infrared light emitting diodes mounted on the implanted micro-drive array. All experiments were conducted under the supervision of the Massachusetts Institute of Technology Committee on Animal Care and followed the guidelines of the US National Institute of Health.

DECODING OF ANIMAL'S POSITION. Data collected in a recording session was divided into a training set for construction of the encoding model, and a testing set for evaluation of the decoding. In both data sets only RUN epochs, when the animals were actively moving along the track at a speed higher than 15 cm/s, were selected for analyses. The stimulus of interest $\boldsymbol{x}$ corresponds to the one-dimensional position of the animals along the track. Only spikes of putative pyramidal cells (spike peak-trough latency > 0.375 ms) that have a minimum peak amplitude of 125 μV were selected for decoding analysis. A four dimensional spike feature vector $\boldsymbol{a}$ was constructed from the spike waveform peak amplitudes on each tetrode. To establish a kernel density based estimate of the rate functions we used a truncated Gaussian kernel (cut-off at 4 standard deviations) for both the spike amplitude dimensions and the position dimension. For spike amplitude an isotropic kernel was used with the same kernel bandwidth in all four dimensions. The rate functions were evaluated at a regular grid with 10 cm intervals that spanned the whole track. For decoding, the testing data set was divided into non-overlapping 250 ms long time bins and spikes within each bin were used to compute the posterior distribution of position according to Eq. (10). A non-informative prior was used, making the

decoding similar to maximum likelihood estimation. The decoding error in each time bin was computed as the absolute difference between the true (observed) position at the center of the time bin and the *maximum a posteriori* (MAP) estimate of position. To assess decoding performance, we analyzed the cumulative distribution of decoding error, the median error and the confusion matrix.

SPIKE SORTING BASED DECODING. For decoding based on sorted units, spikes were manually sorted on the basis of their 4-dimensional peak amplitude vectors using custom software (XClust, M.A.W.). Polygon cluster boundaries were defined using spikes in the training data set; these boundaries were then applied to spikes from the test dataset. Similar to the spike feature based decoding, all spikes were thresholded at 125 μV and only putative pyramidal neurons with a mean spike peak-to-trough latency >0.375 ms were included in the analysis. The spatial tuning curve of each cell was constructed using kernel-density estimation with a truncated Gaussian kernel and a spatial bandwidth that matched the bandwidth used for spike feature based decoding.

RANDOMIZATION. To analyze in more detail the contribution of the association between spike amplitude vectors and position to decoding performance, two randomization procedures were used. For all spikes in the encoding stage, we either shuffled their positions on the track or their associated spike amplitude vectors. A total of 500 independent shuffles were performed to obtain a distribution of median

decoding errors. Based on this distribution, a Monte-Carlo P-value was calculated for the observed median decoding error obtained in the original non-randomized dataset.

RESULTS

A total of 12 datasets from 8 rats were used to test the spike feature based decoding approach. Table 1 summarizes the experimental data and Table 2 tabulates the decoding results, as discussed in more detail below.

Figure 2 shows an example of decoding the position of a rat (dataset SL15, see Table 1) using the peak amplitudes of recorded hippocampal spikes as feature vector. Qualitatively, our estimates of the rat's position on the track accurately follow its true position during periods of locomotion (Fig. 2A-B). To assess the decoding performance, we computed a confusion matrix (Fig. 2C) and the distribution of errors (Fig. 2D). In this example, the median decoding error is 5.4 cm (which is less than the 10 cm sampling interval) and 90% of the errors fall within 19.7 cm. The confusion matrix shows a dominant diagonal structure, which indicates a high accuracy of decoding at most locations along the track.

Choice of the kernel bandwidth

For the kernel density based estimates of the rate functions in the encoding model it is important to select appropriate kernel bandwidth parameters that do not under-smooth nor over-smooth the density. To determine the optimal bandwidths for the spike amplitude and position dimensions, decoding performance was assessed while varying the bandwidth parameters. For the example dataset shown in Figure 2, the combination of bandwidth parameters that minimized the median decoding error

was 30 μV for the spike amplitude and 10 cm for position (Fig. 3). Across all datasets, decoding performance deteriorated rapidly for small bandwidths (below 10 μV and 5 cm) and more gradually for increasing bandwidths. Optimal bandwidth parameters varied between 10 μV and 40 μV for spike amplitude and between 5 cm and 20 cm for position. The bandwidth combination of 30 μV and 10 cm produced (near) optimal decoding performance in all datasets and was therefore used for all subsequent analyses.

Contribution of spike amplitude information

Using the selected bandwidths, the median decoding error across all datasets varied from 5.3 cm to 15.0 cm, with an average median error of 9.1 cm (see Table 2, column 2). To investigate the extent to which spike amplitude information aids in the decoding of position, we compared the performance to a decoder based on spike timing alone using a single spatial tuning curve for each tetrode (multi-unit activity (MUA) decoding; see (Fraser et al., 2009)). In all datasets the error distribution of the MUA decoder is significantly larger than the error distribution of the spike feature based decoder (one-sided two-sample Kolmogorov-Smirnov test, $p < 0.03$ to $p < 6\times10^{-14}$; see example in Fig. 2D). Overall, the median error was significantly reduced when spike amplitude information was included in our spike feature based decoding approach (Fig. 4A; see Table 2, columns 1 and 2; paired rank-sum test, $p = 4.88\times10^{-4}$). To further investigate the contribution of spike amplitude information, we randomly shuffled the amplitude vectors of the spikes in the training set used to

construct the encoding model. In all datasets the median decoding error is significantly lower than what is expected by chance based on 500 shuffles (two-sided Monte Carlo p-value = 0.002; see example in Fig. 2E). After random shuffling of the spike amplitude vectors the decoding performance is worse than when decoding based on multi-unit activity alone (e.g. see Fig. 2E), even though in both cases only spike timing information can be used for decoding. The reason for this discrepancy is that after amplitude randomization, the selected kernel bandwidth of 30 μV is suboptimal (not shown). The decoding performance after shuffling will converge to the performance of the MUA based decoder when the bandwidth for the spike amplitude dimensions is increased towards infinity.

Effect of electrode configuration

Next, we examined the effect of electrode configuration (single-wire electrode, stereotrode or tetrode) on the performance of our spike feature based decoding. This question is motivated by the fact that the use of a particular electrode configuration varies between experiments and is also often correlated with different animal models and brain regions. Single-wire electrode and stereotrode configurations were simulated in our datasets by randomly selecting one or two channels for each tetrode. The spike amplitude threshold of 125 μV was re-applied after the selection, which reduced the total number of spikes used to construct the encoding model to 49.8% ± 10.2% and 71.5% ± 6.2% relative to the tetrode configuration for single wire and stereotrode respectively. The same sets of thresholded spikes were used in

MUA-based decoding for each electrode configuration. The spike amplitude based decoding for the simulated single wire electrode and stereotrode configurations was more accurate than the corresponding MUA decoder that only uses spike timing (one-sided two-sample Kolmogorov–Smirnov test of difference in error distributions, $p < 0.01$). The median decoding error for all data sets and across all electrode configurations is shown in Figure 4B. At the group level, the median error was reduced significantly when comparing stereotrodes to single-wire electrodes (paired rank-sum test, $p = 4.8\times10^{-4}$), or when comparing tetrodes to stereotrodes (paired rank-sum test, $p = 4.8\times10^{-4}$). The relative benefit of stereotrodes over single wire electrodes (range: 9%-65%, mean benefit 35%) was significantly (paired rank-sum test, p=0.0771 and p<.033 two sample KS test) larger than the benefit of tetrodes over stereotrodes (range: 9%-42.6%, mean benefit 24.5%).

Comparison with decoding using sorted single-units

Next, we compared the spike feature decoding approach to the standard practice in which spikes recorded on tetrodes are first sorted into separate single units ("single unit decoder", see (Zhang et al., 1998)). As shown in Table 1, the number of sorted units across all datasets ranges from 9-41, and the fraction of sorted spikes out of all selected putative pyramidal neuron spikes ranges from 3.4% to 64.2%. Most non-sorted spikes had maximum peak amplitude below 200 μV (59.7% to 75.1% of all selected spikes). Thus, the spike feature decoding approach can use information about the stimulus that is carried by spikes in low-amplitude regions, where spike

sorting is difficult or impossible because of the high overlap between individual units and background activity.

At the group level, the spike feature decoder performed significantly better than the decoder based on sorted single units (Fig. 5A; paired rank-sum test, $p = 9.8\times10^{-4}$). The level of performance improvement varied across the datasets. For the subset of datasets with a large number of isolated units (≥ 25 units) the performance of the two decoders was similar (Table 2, bottom 7 datasets; Fig. 5B). In contrast, a large increase in performance was observed for data sets with a low number of isolated units (< 25 units) (Table 2, top 5 datasets; Fig. 5B). Applying the spike feature decoding approach to the subset of successfully sorted spikes only resulted in decoding errors that were comparable to the single unit decoder in all datasets (Fig. 5). This observation indicates that the improved performance of the spike feature decoder is due to the inclusion of non-sorted spikes.

Unsupervised encoding-decoding paradigm

Both encoding and decoding phases of the spike feature decoding paradigm can be performed without supervision. As such, this new paradigm is well suited for online decoding of stimuli from ongoing neural activity as is required for brain-computer interfaces. To demonstrate this we simulate an experiment in which the position of a rat is estimated as it explores a new environment (linear track) for the first time. As soon as the rat enters the new environment, neural data is acquired and for every 250 ms time bin the spikes and their waveform features are used to compute

an estimate of position. If the rat is actively moving (speed > 15 cm/s) in the same time bin, the encoding model is updated using the newly acquired spikes, their waveform features and the rat's physical location in the track. Thus at any given time decoding is performed using only the recorded spike data in the past. Figure 6A shows the position estimates for the first two laps on the track. The estimate of the first lap of behavior is poor as there are only a few source spike events used for the reconstruction. However, this is in stark contrast to the second lap as the position estimate clearly recapitulates the rat's behavior, the median decoding error for the second lap only is 6.1 cm. As the experiment continues each successive lap uses the spikes of all preceding history in the encoding model. The position reconstruction of each lap is accurate as shown by the low median errors (Fig. 6B). These results suggest that only a limited amount of spiking history may be necessary to achieve accurate decoding results when online real-time decoding is required.

DISCUSSION

We have demonstrated a novel Bayesian neural decoding approach that implements a direct mapping between spike waveform features and a sensory stimulus or other covariates. This new approach has several important advantages over other methods. First, the spike feature decoder uses both the timing and waveform features of all available spike events to maximize the amount of stimulus-related information that can be extracted from the neural signals. Second, there is no need for an intermediate spike sorting step that adds complexity and may lead to loss of information. Third, our approach defines a non-parametric encoding model to flexibly describe the relation between the stimulus and neural activity. And finally, the spike feature decoder allows both encoding and decoding stages to be performed without supervision.

We tested the new decoding method on tetrode recordings from the hippocampus in freely behaving rats and showed that the animal's location on a track could be accurately estimated. Our analysis showed that the inclusion of spike waveform features from all four channels on a tetrode resulted in significantly lower decoding errors than (simulated) stereotrode or single wire recordings in the same datasets. Two factors may contribute to this performance increase: a higher number of spike events that meet the peak amplitude threshold on tetrodes and the added spike feature dimensions that increase information content. Even so, if a trade-off has to be made between the number of wires and decoding performance, single wires or

stereotrode may be a good choice and provide better performance than using spike timing alone.

In our tests we used spike peak amplitude as the feature for decoding, however it is possible to use any other set of spike features as well, for example waveform width, wave-shape parameters, or principal components. Our approach takes advantage of the same spike waveform information as most spike sorting methods, but does so without an explicit sorting step. The spike feature decoding approach performs at a similar level as decoding using spike sorted units, when applied to the identical set of (sorted) spike events. However, the new approach can utilize information carried by spikes that cannot be confidently classified as belonging to a single unit. In particular, many low-amplitude spikes that originate from cells far from the electrode are generally not classifiable. Still, these spikes may convey a small amount of information about the stimulus that can be extracted by the decoder. In our tests, we noticed the largest performance gain for data sets in which units were poorly separated.

It is noteworthy to point out the key differences between our approach and other paradigms in which neural spiking data was used for decoding without a spike sorting step. Ventura (2008) proposed a paradigm in which the identities of neurons are extracted implicitly from the spike train recorded on a single electrode by assuming a known parametric model for the neurons' tuning to the stimulus. This

approach worked well in simulations, but was not applied to real data set and it is not clear if the method will work equally well for populations of neurons with complex, non-parametric tuning functions. In addition, the decoding step assumes that the temporal evolution of the stimulus is smooth (Ventura, 2008). This assumption is not necessarily true or known to be true, for example if the goal is to decode a hidden stimulus with unknown temporal dynamics (Davidson et al., 2009; Kloosterman, 2011). In another study, multi-unit activity responses to movement where fitted with a spline function (Fraser et al., 2009) and thus each electrode was treated as a single "virtual" unit. This approach may work well if only a few neurons are recorded on each electrode, or if all neurons contributing to the multi-unit activity have similar tuning properties. However, this method will likely perform poorly if the MUA contains spikes from many neurons with diverse responses, for example in the hippocampus. Stark and Abeles (2007) presented another interesting approach in which multi-unit activity, defined as the root-mean-square of the 300 Hz – 6 kHz band of the local field potential, was used to predict arm movement in monkeys. In this method, spiking activity was not modeled explicitly and decoding was performed by a support vector machine classifier. Unlike our approach, the measure of multi-unit activity in Stark and Abeles (2007) does not separate the contributions of spike rate and amplitude.

The main strength of the proposed spike feature decoding approach is that it provides straightforward stimulus estimation from information-rich spiking data in

an unsupervised manner. The method can be applied in online and real-time encoding/decoding scenarios, which makes it appealing for brain machine interfaces and neural prosthetics that use chronic implants. By utilizing the information carried by all spikes, whether or not they can be uniquely assigned to a single neuron, the spike feature decoding approach is more robust to changes in signal quality as observed in chronic recording applications. In addition, non-stationarity of the neural signals which is commonly encountered in long-term recordings and slow changes in the encoding model can be easily handled by restricting the spike events that contribute to the encoding model to a finite temporal window.

For online applications it is important that the computations for encoding and decoding stages can be performed in real-time. In our current implementation encoding is cheap (all recorded spikes are simply retained), whereas decoding is computationally intensive. The complexity of decoding scales with the total number of spike events incorporated in the encoding model. Several strategies can be used to decrease the computational burden. First, it is possible to exclude spike events based on their waveform properties. For example, in our tests we filtered out spikes with peak amplitude below 125 μV and spikes from putative interneurons. This selection of spikes substantially reduced the computational burden without significantly affecting decoding performance. Another way to alleviate this problem, is to find compact and efficient representations of the kernel density estimates of

the rate functions (Mitra et al., 2002; Girolami, 2003; Zhou et al., 2003; Huang and Chow, 2006).

Our decoding algorithm is based on the statistical assumption that the spike events follow a time-homogeneous spatial-temporal Poisson process (i.e. spike events are mutually independent in both spike feature space and time). This is equivalent to assuming an independent Poisson rate code for all neurons in the ensemble. Although this assumption is over-simplified and unrealistic for experimental data, it provides us with a simple and tractable solution for decoding analysis. [incorporate Sage's suggestion on rate codes here] It is possible to relax the assumptions of Poisson statistics and independence - for example to incorporate temporal dependence the spike history in each electrode can be represented as an augmented temporal feature. Alternatively, the spatial local dependence can be modeled by considering a Neyman-Scott process (Diggle, 2003) or a Poisson cluster process (Bartlett, 1964; Wolpert and Ickstadt, 1998). These topics will be the subject of future investigations.

Our decoding paradigm can be extended in several ways. For instance, we can reformulate the Bayesian decoding problem within the state-space framework by inclusion of a smooth temporal prior (Brown et al., 1998). A temporal prior can be useful for reconstruction of stimuli or covariates that are known to smoothly change over time, such as the position of rat or the movement of an arm. The spike feature

decoding can also be used to extract information from ensemble spiking activity by estimating the mutual information and entropy of the stimulus and neural responses. Estimation of these information measures may provide a better understanding the underlying principles of neural codes used in the brain (Jacobs et al., 2009; Quian Quiroga and Panzeri, 2009).

REFERENCES

Bartlett MS. The spectral analysis of two-dimensional point processes. *Biometrika* 51: 299–311, 1964.

Boloori A-R, Jenks RA, Desbordes G, Stanley GB. Encoding and decoding cortical representations of tactile features in the vibrissa system. *J Neurosci* 30: 9990–10005, 2010.

Brown EN, Frank LM, Tang D, Quirk MC, Wilson MA. A statistical paradigm for neural spike train decoding applied to position prediction from ensemble firing patterns of rat hippocampal place-cells. *J Neurosci* 18: 7411–25, 1998.

Chapin JK. Using multi-neuron population recordings for neural prosthetics. *Nat Neurosci* 7: 452–5, 2004.

Davidson TJ, Kloosterman F, Wilson MA. Hippocampal replay of extended experience. *Neuron* 63: 497–507, 2009.

Diggle PJ. *Statistical Analysis of Spatial Point Patterns*. 2nd ed. Oxford University Press, 2003.

Fraser GW, Chase SM, Whitford A, Schwartz AB. Control of a brain-computer interface without spike sorting. *J Neural Eng* 6: 055004, 2009.

Georgopoulos a P, Schwartz a B, Kettner RE. Neuronal population coding of movement direction. *Science* 233: 1416–9, 1986.

Girolami M. Probability density estimation from optimally condensed data samples. *IEEE Transactions on Pattern Analysis and Machine Intelligence* 25: 1253–1264, 2003.

Goodman IN, Johnson DH. Information theoretic bounds on neural prosthesis effectiveness: The importance of spike sorting. In: *2008 IEEE International Conference on Acoustics, Speech and Signal Processing*. IEEE, p. 5204–5207.

Gupta AS, van der Meer M a a, Touretzky DS, Redish a D. Hippocampal replay is not a simple function of experience. *Neuron* 65: 695–705, 2010.

Hochberg LR, Bacher D, Jarosiewicz B, Masse NY, Simeral JD, Vogel J, Haddadin S, Liu J, Cash SS, van der Smagt P, Donoghue JP. Reach and grasp by people with tetraplegia using a neurally controlled robotic arm. *Nature* 485: 372–5, 2012.

Huang D, Chow TWS. Enhancing density-based data reduction using entropy. *Neural Comput* 18: 470–95, 2006.

Huys QJM, Zemel RS, Natarajan R, Dayan P. Fast population coding. *Neural Comput* 19: 404–41, 2007.

Jacobs AL, Fridman G, Douglas RM, Alam NM, Latham PE, Prusky GT, Nirenberg S. Ruling out and ruling in neural codes. *Proc Natl Acad Sci U S A* 106: 5936–41, 2009.

Kloosterman F, Davidson TJ, Gomperts SN, Layton SP, Hale G, Nguyen DP, Wilson MA. Micro-drive array for chronic in vivo recording: drive fabrication. *J Vis Exp* , 2009.

Kloosterman F. Analysis of Hippocampal Memory Replay Using Neural Population Decoding. *Neuronal network analysis: concepts and experimental approaches. (Neuromethods)* : 259–282, 2011.

Mitra P, Murthy C, Pal S. Density-based multiscale data condensation. *IEEE Transactions on Pattern Analysis and Machine Intelligence.* 24: 734–747, 2002.

Nguyen DP, Layton SP, Hale G, Gomperts SN, Davidson TJ, Kloosterman F, Wilson MA. Micro-drive array for chronic in vivo recording: tetrode assembly. *J Vis Exp* , 2009.

Paninski L, Pillow J, Lewi J. Statistical models for neural encoding, decoding, and optimal stimulus design. *Prog Brain Res* 165: 493–507, 2007.

Quian Quiroga R, Panzeri S. Extracting information from neuronal populations: information theory and decoding approaches. *Nat Rev Neurosci* 10: 173–85, 2009.

Sanger T. Neural population codes. *Current Opinion in Neurobiology* 13: 238–249, 2003.

Schwartz AB, Cui XT, Weber DJ, Moran DW. Brain-controlled interfaces: movement restoration with neural prosthetics. *Neuron* 52: 205–20, 2006.

Stark E, Abeles M. Predicting movement from multiunit activity. *J Neurosci* 27: 8387–94, 2007.

Truccolo W, Eden UT, Fellows MR, Donoghue JP, Brown EN. A point process framework for relating neural spiking activity to spiking history, neural ensemble, and extrinsic covariate effects. *J Neurophysiol* 93: 1074–89, 2005.

Ventura V. Spike train decoding without spike sorting. *Neural Comput* 20: 923–63, 2008.

Wolpert R, Ickstadt K. Poisson/gamma random field models for spatial statistics. *Biometrika* 85: 251–267, 1998.

Wood F, Black MJ. A nonparametric Bayesian alternative to spike sorting. *J Neurosci Methods* 173: 1–12, 2008.

Zhang K, Ginzburg I, McNaughton BL, Sejnowski TJ. Interpreting neuronal population activity by reconstruction: unified framework with application to hippocampal place-cells. *J Neurophysiol* 79: 1017–44, 1998.

Zhou A, Cai Z, Wei L, Qian W. M-kernel merging: towards density estimation over data streams. In: *Eighth International Conference on Database Systems for Advanced Applications, 2003. (DASFAA 2003). Proceedings*. IEEE, p. 285–292.

Zhuang J, Truccolo W, Vargas-Irwin C, Donoghue JP. Decoding 3-d reach and grasp kinematics from high-frequency local field potentials in primate primary motor cortex. *IEEE Trans Biomed Eng* 57: 1774–84, 2010.

Table 1. Summary of experimental data (ranked by # sorted units)

Dataset	# Tetrodes	# Spikes (total)	# Spikes (sorted)	% Sorted Spikes	# Sorted Units
R1d2	12	33 K	7.8K	23.4%	9
R2d2	12	32 K	6.0K	18.8%	9
R1d1	12	185 K	6.4K	3.5%	10
FK11	9	197 K	21 K	10.7%	13
R2d1	12	175 K	11 K	6.5%	14
Sat2	18	790 K	82 K	10.4%	26
Esm02	18	364 K	43 K	11.8%	28
Esm01	18	416 K	39 K	9.4%	30
SL13	24	139 K	48 K	34.5%	35
SL16	24	188 K	39 K	20.7%	36
SL14	24	148 K	34 K	22.8%	40
SL15	24	250 K	52 K	20.8%	41

Table 2. Summary of decoding performances across all datasets (ranked by #sorted units)

Dataset	MUA decoder median error (cm)	feature decoder (tetrode) median error (cm) [% improvement over MUA decoder]	feature decoder (stereotrode) median error (cm) [rel. benefit of tetrode vs. stereotrode]	feature decoder (single wire) median error (cm) [rel. benefit of stereotrode vs. single wire]	single unit decoder median error (cm) [% improvement over MUA decoder]	feature decoder (tetrode) % improvement over single unit decoder
R1d2	85.3	13.1 [84.6%]	22.8 [42.6%]	65.6 [65.2%]	37.5 [56.0%]	65.1%
R2d2	74.1	13.2 [82.2%]	20.8 [36.5%]	61.0 [66.0%]	51.2 [30.9%]	74.3%
R1d1	43.1	14.0 [67.5%]	23.8 [41.1%]	34.8 [31.7%]	54.1 [-25.5%]	74.1%
FK11	31.5	7.6 [75.8%]	12.4 [38.7%]	18.3 [32.0%]	13.6 [56.8%]	44.1%
R2d1	39.7	15.0 [62.3%]	25.8 [42.1%]	36.4 [29.1%]	61.8 [-55.7%]	75.8%
Sat2	47.0	8.9 [81.1%]	10.1 [11.9%]	22.9 [55.9%]	14.8 [68.4%]	40.0%
Esm02	12.9	5.3 [58.8%]	6.7 [21.0%]	8.7 [22.7%]	8.2 [36.2%]	35.4%
Esm01	24.1	7.6 [68.3%]	8.9 [14.4%]	12.3 [27.2%]	10.4 [57.1%]	26.3%
SL13	29.4	7.7 [73.8%]	8.9 [13.2%]	14.0 [36.6%]	8.6 [70.7%]	10.3%
SL16	21.9	5.6 [74.6%]	6.4 [12.7%]	8.4 [24.2%]	7.2 [67.3%]	22.3%
SL14	12.1	6.1 [50.0%]	6.7 [9.0%]	8.1 [17.8%]	5.9 [51.6%]	- 3.4%
SL15	15.2	5.4 [64.3%]	6.4 [15.4%]	8.0 [20.1%]	6.8 [55.2%]	20.3%

FIGURE LEGENDS

Figure 1. Diagram of spike waveform feature decoding approach. In the encoding stage (left), a model describing the relation between spike waveform features and the stimulus of interest (for example an animal's position) is constructed. Note that no prior sorting of the recorded spikes is required. In the decoding stage (right), the encoding model is used to obtain an estimate of the stimulus from the measured spike waveform features.

Figure 2. Example of spike waveform feature decoding of a rat's position on a 3 meter long track (dataset SL15). **A.** Posterior probability distributions of the decoded position along the track for an epoch spanning multiple laps. Darker shades of gray indicate higher probabilities. Posterior distributions are computed for non-overlapping 250 ms long time bins. The red line represents the rat's actual position on the track. **B.** Detailed view of the decoded trajectory for a single lap (first lap in A). **C.** Confusion matrix showing the distribution of estimated positions for all positions on the track. **D.** Empirical cumulative distribution function (CDF) of decoding errors for dataset SL15. Red: spike waveform feature decoder. Black: MUA decoder. Blue dashed line marks the 90% error percentile for the feature decoder. Inset shows detail of the CDFs. **E.** Median error statistics for the spike waveform feature decoder (red) and MUA decoder (black). In blue, the distribution of median errors obtained after randomizing the original spike amplitude vectors (n=500 randomizations).

Figure 3. Effect of kernel bandwidths on decoding performance. The median decoding error for one dataset (SL15) is color coded and plotted as function of the kernel bandwidths for position and spike amplitude. The lowest median error is associated with a bandwidth of 30 μV (spike amplitude) and 10 cm (position) as highlighted by the intersecting white rectangles. Plots on the left and top show a cross-section of the full matrix at the optimal bandwidths.

Figure 4. Population summary statistics of the spike waveform feature decoder. **A.** Box plots comparing the distributions of median errors across all datasets for the spike waveform feature decoder and the MUA decoder. Gray lines represent data of all individual datasets. **B.** Box plots comparing the median error distributions across all datasets for three electrode configurations: single wires, stereotrodes and tetrodes. Gray lines represent data of all individual datasets.

Figure 5. Comparison of the spike waveform feature decoder to the standard single unit decoder. **A.** Box plots comparing the distributions of median errors across all datasets for three different decoding scenarios: feature decoder using all spikes (left) or only the sorted spikes (middle) and a single unit decoder (right). **B.** Scatter plot of median decoding errors in all datasets for the single unit decoder versus the median decoding errors for the spike waveform feature decoder (black: all spikes, grey: sorted spikes). Datasets with fewer than 25 sorted units are indicated by crosses.

Note the large reduction in median decoding error for datasets with < 25 units when all spikes are included in the encoding and decoding stages.

Figure 6. Simulated unsupervised online decoding. **A.** Posterior probability distributions for 250 ms time bins in two epochs corresponding to the first two laps on the track. Darker shades of gray indicate higher probabilities. The red line represents the rat's actual position on the track. **B.** Median decoding error computed for each lap separately. The horizontal dashed line shows the mean of the median decoding error statistics across all laps

.

FIGURES

FIGURE 1

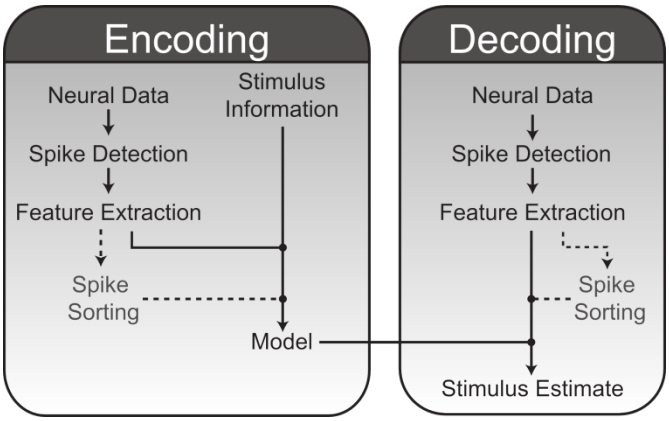
Encoding
Neural Data
Stimulus Information
Spike Detection
Feature Extraction
Spike Sorting
Model
Decoding
Neural Data
Spike Detection
Feature Extraction
Spike Sorting
Stimulus Estimate

FIGURE 2

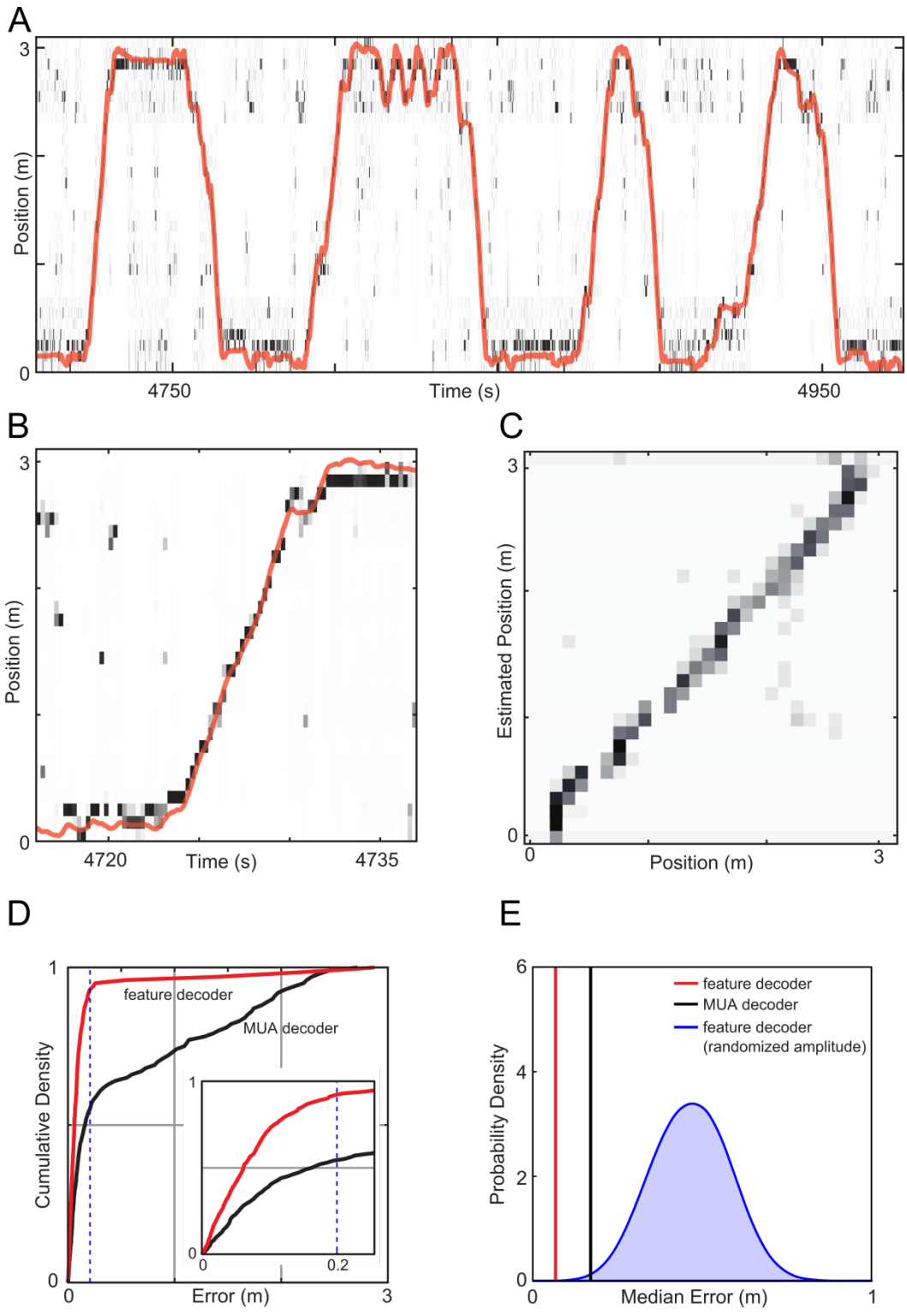
A
3
Position (m)
0
4750
Time (s)
4950
B
3
Position (m)
0
4720
Time (s)
4735
C
3
Estimated Position (m)
0
0
Position (m)
3
D
1
Cumulative Density
0
feature decoder
MUA decoder
1
0
0
0.2
0
Error (m)
3
E
6
Probability Density
4
2
0
feature decoder
MUA decoder
feature decoder
(randomized amplitude)
0
Median Error (m)
1

FIGURE 3

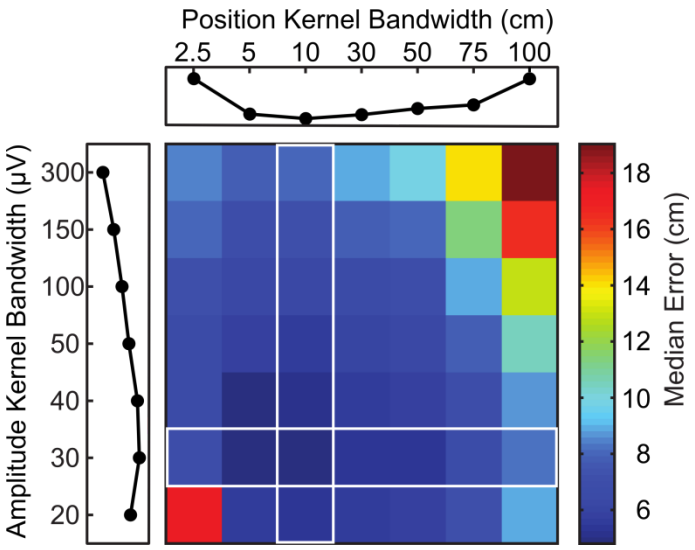
Position Kernel Bandwidth (cm)
2.5
5
10
30
50
75
100
Amplitude Kernel Bandwidth (μV)
300
150
100
50
40
30
20
Median Error (cm)
18
16
14
12
10
8
6

FIGURE 4

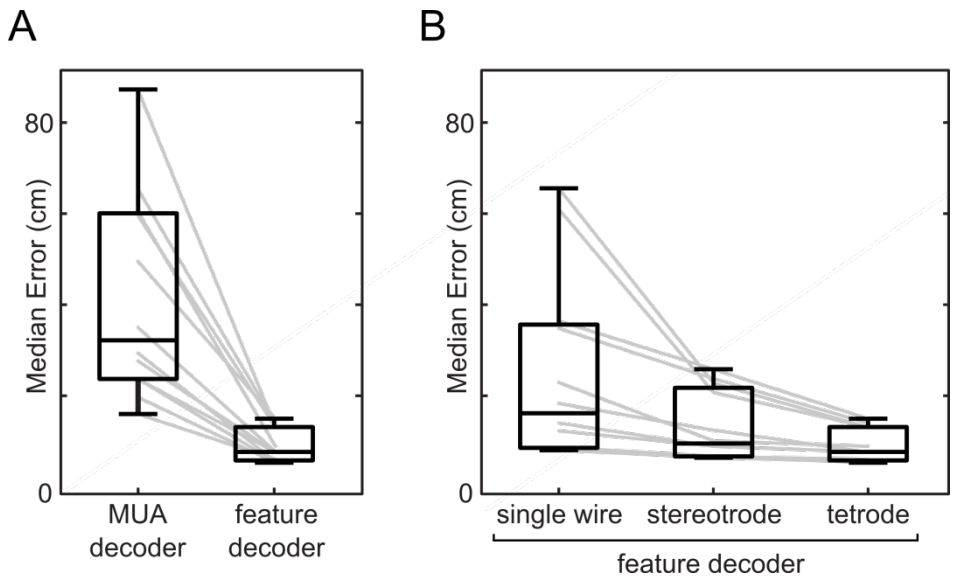
A
B
80
0
Median Error (cm)
MUA
decoder
feature
decoder
single wire
stereotrode
tetrode
feature decoder

FIGURE 5

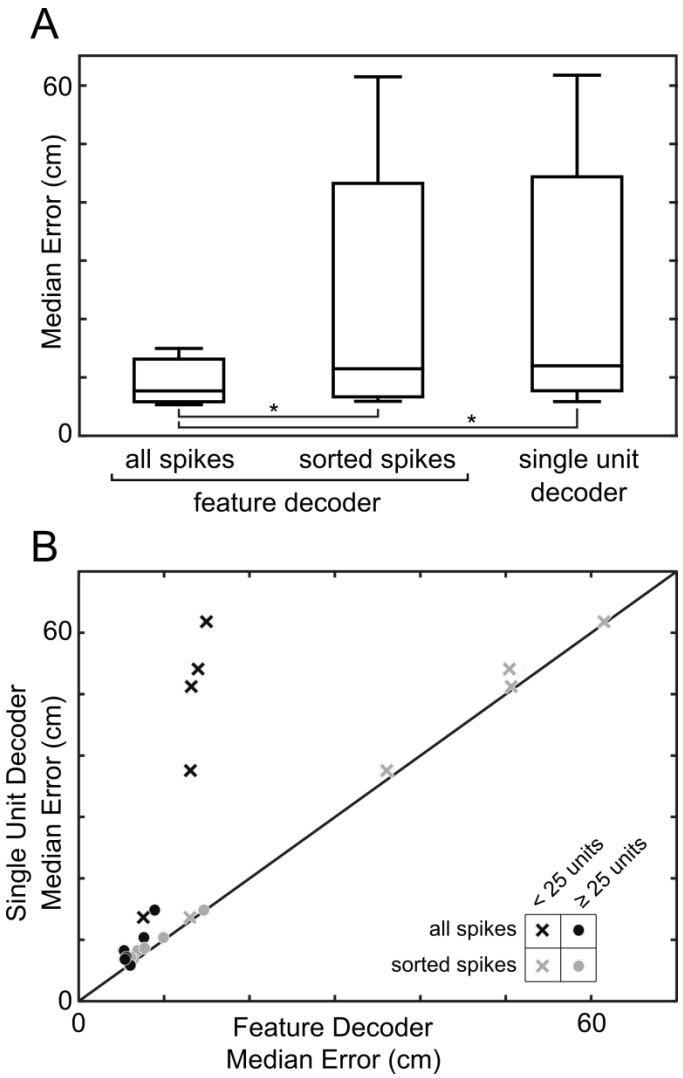
A
60
0
Median Error (cm)
*
*
all spikes
sorted spikes
feature decoder
single unit
decoder
B
60
0
Single Unit Decoder
Median Error (cm)
0
60
Feature Decoder
Median Error (cm)
< 25 units
≥ 25 units
all spikes
sorted spikes

FIGURE 6

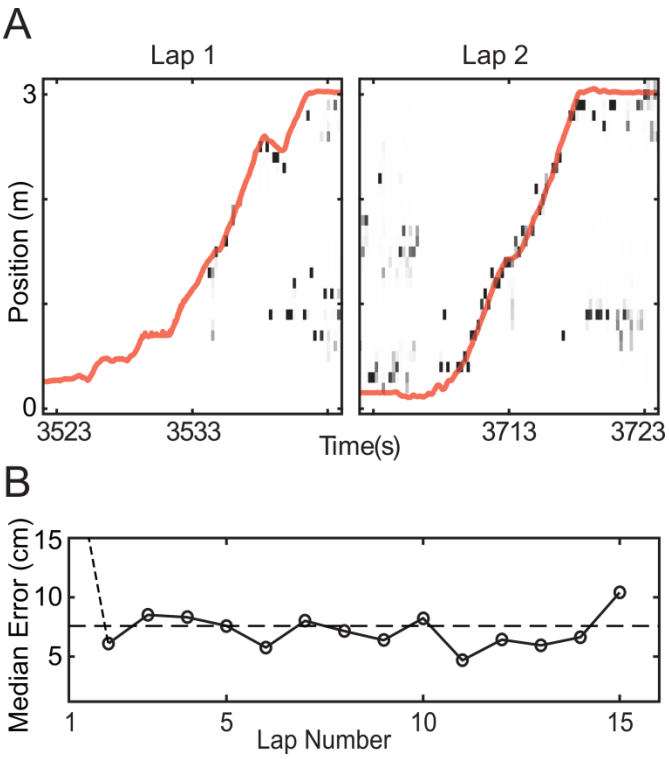
A
Lap 1
Lap 2
3
0
Position (m)
3523
3533
Time(s)
3713
3723
B
Median Error (cm)
15
10
5
1
5
10
15
Lap Number

Discussion

Models of Ripple Chain Generation

A popular model of episodic memory formation theorizes that during experience, or learning, information from the periphery is encoded and processed by the neo-cortex. However, long-term memories are not consolidated during the encoding stage but rather cortical information is passed to the hippocampus for short-term retention. The hippocampus then rapidly forms short-lived (days to months) representations of the cortical information.

During off-line periods, such as sleep, representations stored by the hippocampus are passed back to cortex and consolidated into memories that can persist for long periods of time (years to decades). These cortically encoded memories form slower than their hippocampal counterparts but can persists for years or decades.

The electrophysiology of the hippocampus and particularly the phenomenon of hippocampal replay are explained by this model well. In-deed replay is a candidate mechanism by which hippocampal information returns to cortex for long-term consolidation. However, an alternative hypothesis for hippocampal replay suggests that rather than representing the information transfer from the hippocampus to cortex, replay is a part of the mechanism responsible for maintaining short-lasting hippocampal representations. This model claims that without replay, hippocampal representations would quickly deteriorate.

Early work on HPC reactivation demonstrated that replay occurred during sharp-wave ripples in the HPC local-field potential. Initially it was thought that ripples corresponded to individual replay events, however, it has recently been demonstrated that replay evens can span multiple individual ripples suggesting the existence of ripple sets or chains. Specifically, it was determined that representations encoded by the hippocampus during replay are coherent across ripple events that are adjacent in time. These findings provide evidence that while ripples can be thought of as individual events, at some level information is being coordinated for the duration of a ripple event chain.

The mechanisms responsible for chaining individual ripples together in both time and content are unknown. Here we propose two candidate mechanisms for chaining individual ripple events into longer event sets.

Hippocampal Cortical Reciprocal Model

The first model (**Figure 1**), which we call the reciprocal model, relies upon interactions between the neo-cortex and the hippocampus. Replay events are initiated by cortex, which determines what information should be replayed and then provides feed-forward drive into the hippocampus, which triggers a single, ripple event in conjunctions with replay of the cortically specified content. Following the successful generation of a ripple with the appropriate content, cortex reacts by providing additional drive into the hippocampus, which triggers subsequent

ripple/replay events. The back-and-forth between cortex and the hippocampus can continue as long as the two structures are synchronized.

This model makes specific prediction about cortical activity during ripple chains. First it predicts the existence of some cortical activity that precedes each ripple in a ripple chain. Second it predicts that the timescale on which this putative activity operates are congruent with the time-scale on which ripple events are generated. More specifically, cortical drive should be observable, in some form, for each ripple event and the time between periods of cortical drive should reflect the time periods between ripple events.

Next it suggests disrupting drive into the hippocampus, while sparing hippocampal activity, would be sufficient to disrupt ripple-chains. Likewise disruption of the hippocampus, but not cortex, between ripples events should not disrupt the generation of ripple chains.

Intrinsic Hippocampal Model

An alternative model, called the intrinsic model (**Figure 2**), depends on the feedback circuitry contained within the hippocampal formation. Like with the reciprocal model, the initial ripple in a ripple-chain is triggered by cortical drive; however, subsequent ripples are triggered through the hippocampal feedback circuitry in the hippocampus.

This model, like the reciprocal model, predicts cortical activity correlated with the first ripple in a ripple chain; however, during cortical activity would be de-correlated with subsequent ripples in the same chain.

The intrinsic model can be used to predict the result of hippocampal and cortical disruption on ripple event chains. As circuits contained entirely within hippocampus are hypothesized to generate ripple chains, disruption of cortical activity of should have little to no effect on production ripple chains. Conversely, disruption of hippocampal activity between ripples could disrupt the chaining process.

In an attempt to examine the validity of these two models, we investigated the ripple-associated activity in cortical multi-unit activity (MUA). We hypothesized that we might observe activity that was correlated with the on set of ripple chains indicating cortical drive triggering the on set of ripple chains. Furthermore, we examined the cortical MUA for the complete duration of ripple-chains, hoping to determine if cortical activity is correlated with each ripple event or only the first event in the chain.

Electrophysiological Evidence Supporting the Models

We analyzed ripple-associated activity of the retrosplenial cortex (RSX) in the rat looking for evidence of either model. RSX was chosen over other cortical areas, such as M1 or S1, for several reasons. First RSX has strong reciprocal connections with the hippocampus. Second lesions to RSX induce a form of retrograde amnesia that resembles the type of amnesia observed in patients with HPC damage. Additionally, a subpopulation of neurons in RSX has spatial tuning properties related to the tuning properties of neurons in the hippocampal formation.

Prior to ripples in CA1 we observed an increase in the multi-unit activity (MUA) in RSX and is dramatically suppressed during the ripple event. In the case of ripple doublets, RSX MUA increases a second time; however, the distance between peaks in the RSX MUA is roughly 100ms. The timescale of activity we observe during ripple doublets in RSX does not line up with the time-scale of HPC ripple associated activity. These results provide evidence for both models. First activity in RSX precedes ripples in the HPC and in the case of ripple doublets we see a second burst of activity in RSX; however, the time-scale do not align.

We hypothesized that perhaps both models might be operating and that the interval between adjacent ripples in a doublet might indicate which model is dominating ripple generation at any given time. We observed that the ripple associated MUA in RSX varied greatly depending on the time-interval between ripples in the same doublet. In the case short interval doublets we observed activity in RSX prior to the

first ripple; however, for the remainder of the doublet the MUA activity in RSX remained suppresser. Conversely, for the long interval doublets we observed a strong recovery in the MUA of RSX followed by a second round of inhibition. Again the distances between the peaks of MUA in RSX was ~100ms. This timescale corresponds with what the HPC MUA associated with long and short interval doublets. The HPC MUA is increases during ripple events, in the case of short-interval doublets the time-intervals between peaks in the HPC MUA are short while longer inter-ripple-intervals yield longer inter-MUA-peak-intervals. However, only in the case of long-interval doublets do the timescale of activity in RSX and HPC align.

These results provide evidence that both hippocampal-cortical interactions and internal hippocampal circuitry are involved in the generation of ripple-event chains. Furthermore, our results indicate that the intervals between ripples within a ripple chain indicate which model may be more active at any given time. This is interesting as it supports a dual role for hippocampal replay. Further work should be done to evaluate these models and results.

FIGURES

Figure 1.

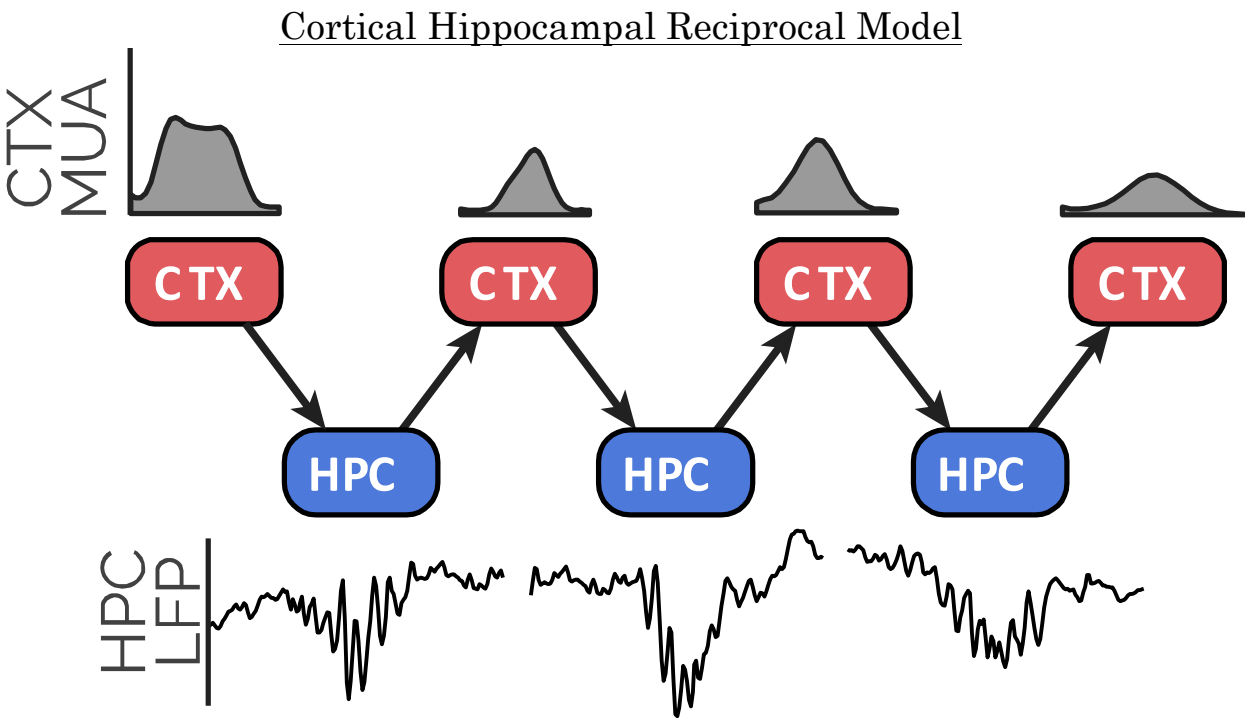

Figure 2.

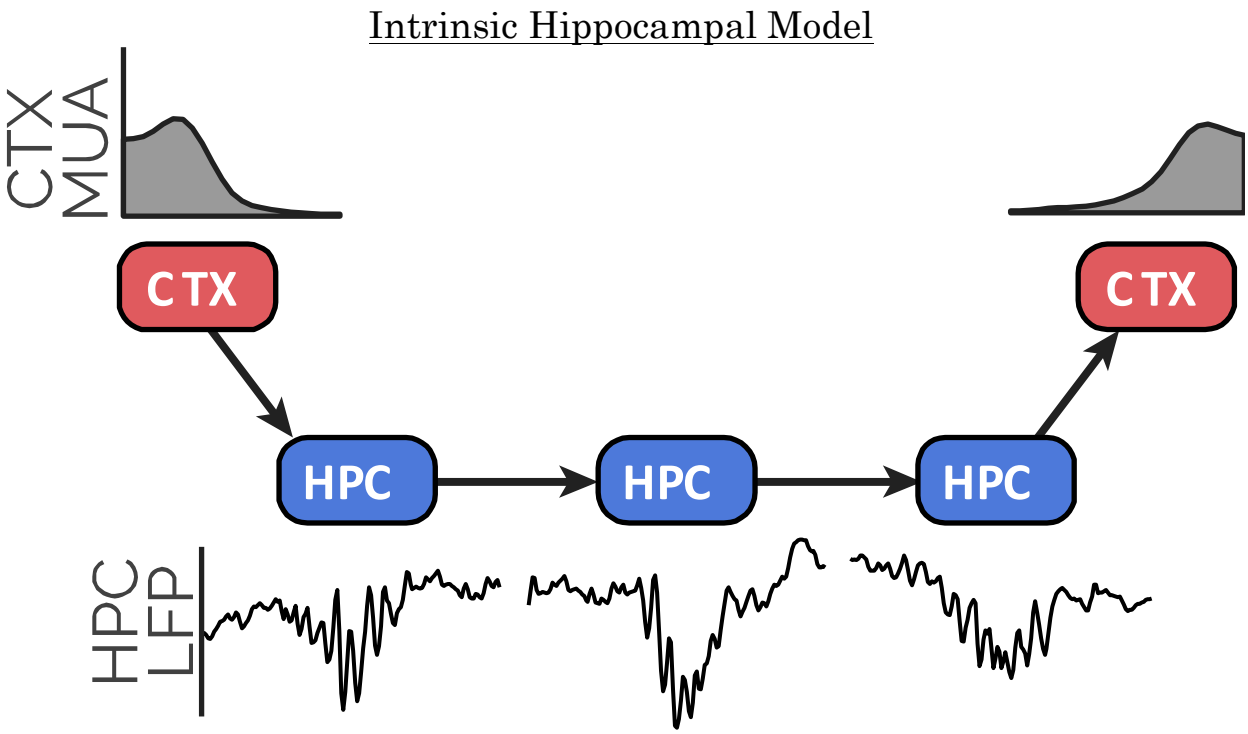
Intrinsic Hippocampal Model
CTX MUA
CTX
CTX
HPC
HPC
HPC
HPC LFP

Declaration of Contributions

Chapter 2:

- Dr. Loren Frank and his Lab at UCSD graciously provided the data for one of the animal.
- Stuart P. Layton collected data from the other two animals, performed all of the analysis and prepared the entire manuscript.

Chapter 3:

- Dr. Hector Penagos and Greg Hale graciously provided all of the data presented in this chapter
- Stuart P. Layton performed all of the analysis and prepared the entire manuscript.

Chapter 4:

- The method presented in this chapter was chiefly developed by Dr. Fabian Kloosterman . Dr. Kloosterman oversaw the preparation of the manuscript and is the author of a substantial fraction of the text.
- Dr. Zhe Chen, aided in technical development and in the preparation of the manuscript.
- Stuart P. Layton performed all of the analysis presented in this chapter, prepared the majority of the figures and contributed to the Methods and Results sections of this manuscript.